City, University of London Institutional Repository

This is the accepted version of the paper.

This version of the publication may differ from the final published version.

Numerical investigation of bubble dynamics using tabulated data

Nikolaos Kyriazis [a], Phoevos Koukouvinis [a] and Manolis Gavaises [a]

[a] *School of Mathematics, Computer Science & Engineering, Department of Mechanical Engineering & Aeronautics, City University London, Northampton Square EC1V 0HB, United Kingdom*

Abstract

An explicit density-based solver of the compressible Euler equations suitable for cavitation simulations is presented, using the full Helmholtz energy Equation of State (EoS) for n-Dodecane. Tabulated data are derived from this EoS in order to calculate the thermodynamic properties of the liquid, vapour and mixture composition during cavitation. For determining thermodynamic properties from the conservative variable set, bilinear interpolation is employed; this results to significantly reduced computational cost despite the complex thermodynamics model incorporated. The latter is able to predict the temperature variation of both the liquid and the vapour phases. The methodology uses a Mach number consistent numerical flux, suitable for subsonic up to supersonic flow conditions. Finite volume discretization is employed in conjunction with a second order Runge-Kutta time integration scheme. The numerical method is validated against the Riemann problem, comparing it with the exact solution which has been derived in the present work for an arbitrary EoS. Further validation is performed against the well-known Rayleigh collapse of a pure vapour bubble. It is then used for the simulation of a 2-D axisymmetric n-Dodecane vapour bubble collapsing in the proximity of a flat wall placed at different locations from the centre of the bubble. The predictive capability of the incorporated Helmholtz EoS is assessed against the widely used barotropic EoS and the non-isothermal Homogeneous Equilibrium Mixture (HEM).

Keywords: Bubble dynamics, cavitation, Helmholtz equation of state, exact Riemann solver

Nomenclature

$\mathbf{U}$	Conservative variable vector
$\mathbf{F}$	r-flux vector
$\mathbf{G}$	z-flux vector
$\mathbf{S}$	Geometric source vector
ρ	Density (kg/m^3)
u_r	Velocity in the r-direction (m/s)
u_z	Velocity in the z-direction (m/s)
p	Pressure (Pa)
e	Internal energy (J/kg)
e_{liq}	Internal energy of the liquid (J/kg)
e_{vap}	Internal energy of the vapour (J/kg)
E	Total energy (J/kg)
s	Geometric source term, unity for cylindrical symmetry and two for spherical symmetry (-)

47	r	Distance from the axis/point of symmetry, needed in the geometric source term (m)
48	**n**	Normal surface vector
49	a	Molar Helmholtz energy (J)
50	a^0	Ideal gas contribution to the Helmholtz energy (J)
51	a^r	Residual Helmholtz energy, responsible for the influence of Intermolecular forces (J)
52	α^0	Dimensionless ideal gas contribution to the Helmholtz energy (-)
53	α^r	Dimensionless residual Helmholtz energy (-)
54	p_c	Critical pressure (Pa)
55	ρ_c	Critical density (kg/m^3)
56	p_{sat}	Saturation pressure (Pa)
57	$\rho_{sat,L}$	Liquid density at saturation (kg/m^3)
58	$\rho_{sat,V}$	Vapour density at saturation (kg/m^3)
59	B	Liquid bulk modulus (Pa)
60	C	Speed parameter (Pa·kg/m^3)
61	n	Tait equation parameter, equal to 7.15 for weakly compressible liquids (-)
62	T_0	Initial temperature (K)
63	C_{vl}	Specific heat at constant volume for the liquid (J/(kg·K))
64	C_{vv}	Specific heat at constant volume for the vapour (J/(kg·K))
65	e_{l0}	Internal energy at reference temperature T_0 (J/kg)
66	L_v	Latent heat (J/(kg·K))
67	R	Specific gas constant (J/(kg·K))
68	γ	Ratio of specific heats (-)
69	N_{mn}	Finite element nodal shape function of node n, evaluated at node m (-)
70		

1. Introduction

Many studies deal with the dynamics of vapour bubbles, both computationally and experimentally, due to the implications they have in a number of physical conditions and technological applications. Up to now, different approaches have been proposed for simulating bubble collapse dynamics, such as potential flow solvers with dynamic boundary conditions on the bubble surface, homogeneous mixture models and interface tracking/capturing methods.

Methodologies based on potential flow solvers have been among the first employed to simulate the collapse of bubbles. For example, Plesset and Chapman (1971) were the first to study cavitation bubble collapse close to a solid surface. A potential flow solver was used for the liquid phase and a Marker-and-Cell technique was developed for tracking the bubble interface. A similar flow solver was employed by Zhang et al. (1993), (1994) but a Boundary Element Method was incorporated for predicting the shape of the bubble and the pressure profile on the wall. In an extension of the BEM method, Wang (2014) employed a combination of compressible and incompressible potential flow for the simulation of a bubble collapse in the vicinity of a wall, aiming to describe the energy loss due to pressure waves radiated during the bubble collapse. The advantage of the BEM methodology is that only the bubble interface is discretized and resolved, transforming the 3D problem to a 2D one. However, mesh handling is problematic when topological changes of the bubble interface have to be taken into consideration, e.g. during bubble jet formation or impact on walls. For that reason, Chahine (2014) used a coupling between an incompressible BEM potential flow solver and a multiphase compressible flow solver based on the Euler equations for simulating the growth and collapse of a bubble in the vicinity of (deformable) walls. Each solution strategy was employed at different stages of the bubble development; for the violent growth

and collapse of the simulated bubble the compressible multiphase approach was used, whereas the BEM method was employed at intermediate stages where flow velocities are small.

Adams and Schmidt (2013) used a single fluid model and simulated the collapse of a bubble cluster consisting of 125 bubbles. The model was based on the Equation of State (EoS) for the pure phases, and thus, no empirical parameters and tuning were needed. The main assumption in this model is that the two-phase regime is in thermodynamic and mechanical equilibrium. Although this assumption may not be valid in metastable thermodynamic states, the model is accurate enough for medium and large scale simulations of cavitating flows. A similar work by Schmidt et al. (2008) emphasized on the detection of the shock formation and propagation in three dimensional cloud cavitation. Despite the limitation of not explicitly defining the bubble interface, such models are still widely used due to their simplicity; this limitation has been proved not to be important, since the bubble interface can be estimated by the density variation when using an adequate cell resolution. Since the bubble interface may be somewhat diffuse, surface tension is commonly neglected. In any case the effect of this assumption is minor, since surface tension plays a minor role during bubble collapse, which is mainly governed by inertia.

Overcoming the limitation of the previous methods, front tracking methods, which have been originally developed by Glimm et al. (1985) and a follow-up study by Unverdi and Tryggvason (1992), offer higher accuracy in resolving the exact bubble shape. For example, the Lagrangian method of Hawker and Ventikos (2009), (2012) used a marker to track the liquid-gas interface; the computational mesh was divided in two regions, with different EoS applied for the two phases. In addition, Popinet et al. (2002) used a front-tracking approach while free surface boundary conditions were imposed for simulating bubble flows near solid boundaries. The main advantage of this methodology is that it allows for smear-free interfaces, resulting in sharp interfaces for large scale problems and can model diffuse interfaces in smaller scales. Another feature of the front-tracking method is that it can be applied to complex geometries while it allows for large deformations of the surface to be simulated. The main drawback of front-tracking methods is their complexity, since the interface grid must be dynamically reconstructed, either adding or removing nodes in areas of stretched or compressed cells, respectively (Unverdi and Tryggvason, 1992).

Interface capturing schemes based on the VOF methodology have been also employed to the simulation of cavitation bubbles. For example, Li et al. (2014) investigated the bubble collapse near a conical rigid boundary, formulating an extension to the classical Rayleigh collapse time, incorporating the wall stand-off distance and the cone angle. Koukouvinis et al. (2016b), (2016c) investigated the effect of asymmetries (e.g. pressure gradient and free surfaces) affecting the bubble collapse, using the VOF technique, and demonstrating jetting effects and bubble shape at collapse stages. Hu et al. (2006) developed a conservative interface method based on the level set technique for solving compressible multiphase flows, maintaining a sharp liquid-gas interface. The methodology was tested in fundamental shock tube cases, bubble-shock wave interactions and underwater explosions. In connection to the previous work, Lauer et al. (2012) used a Level-Set method for bubble dynamics, including non-equilibrium thermodynamic effects and finite mass transfer based on the Hertz-Knudsen relation, while exploring the effect of the wall distance on the bubble shape during collapse; this methodology is also discussed in Adams and Schmidt (2013). While admittedly the discussed interface capturing methodologies can provide a sharp interface, the concept of "interface capturing" is questionable when pressures reach close to the critical point, since

142 liquid and vapour densities become similar and surface tension diminishes, preventing a clear
143 distinction between the two phases.

144   In the previous studies, thermal effects are typically ignored or are considered utilising
145 simplified EoS. In two-fluid models that utilise interface capturing methods, the common
146 assumption is to prescribe a finite mass transfer rate across the bubble interface, describing
147 the evaporation and condensation processes. On the other hand, in single-fluid models
148 mechanical and thermal equilibrium is assumed and the mass transfer is assumed to be
149 infinite. A subcategory of the latter is the barotropic cavitation model, where the pressure is
150 linked to density only, ignoring the effect of temperature; such models have been successfully
151 used for the prediction of cavitation either on macroscopic (e.g. hydrofoils (Dular and
152 Coutier-Delgosha, 2009), venturi (Decaix and Goncalvès, 2013), or high pressure throttle
153 flows (Koukouvinis and Gavaises, 2015)), or single bubble collapses (Koukouvinis et al.,
154 2016a).

155   The current study expands the previous work of Koukouvinis et al. (2016a) where
156 central upwind schemes were used for bubble dynamics simulations, following an isentropic
157 process assumption and using a 2 step barotropic EoS. Comparing with the aforementioned
158 study, in the current work we aim to examine heating effects during the collapse of a
159 vaporous bubble, which have been omitted or simplified in previous studies. The
160 thermodynamic closure used is based on the Helmholtz energy EoS from NIST Refprop
161 databases (Lemmon and Huber, 2004), which can provide thermodynamic properties at
162 subcritical and supercritical conditions in a consistent framework. It is highlighted that in
163 reality bubbles contain an amount of non-condensable gases, which in the present study has
164 been omitted. However, our interest is to examine the temperature changes of the dodecane
165 liquid, due to the extreme pressurisation during bubble collapse.

166   The homogeneous equilibrium model (HEM) approach is used, where each
167 thermodynamic property can be expressed as a function of density and internal energy.
168 Following the methodology of Dumbser et al. (2013), tabulated EoS are employed in the
169 present explicit density-based algorithm; the low Mach number problem is tackled by the
170 hybrid flux model of Schmidt et al. (2008). By using the Helmholtz EoS, a complex
171 thermodynamic model is incorporated in the finite volume solver, while the tabulated data
172 algorithm is proved to be more efficient than using iterative property calculation methods for
173 each time step. To the author's best knowledge, this is the first work implementing the Mach
174 consistent numerical flux in connection with real fluid properties for n-Dodecane,
175 demonstrating heating effects in bubble collapse cases; the only relevant work is that of
176 Dumbser et al. (2013), who focused instead on water/vapour behaviour in benchmark (e.g.
177 shock tube, explosion/implosion, forward step) and macroscopic (e.g. hydrofoil) cases.

178   The paper is organized as follows. In section 2 the numerical method is presented,
179 including the EoS representing the thermodynamic properties of n-Dodecane and time/space
180 discretization methods employed. In section 3 the results are presented and discussed.
181 Validation of the numerical method is performed against the exact solution of the Riemann
182 problem for the EoS under consideration. Further validation is performed against the
183 benchmark Rayleigh vapour bubble collapse. Then several bubble configurations of vapour
184 bubble collapse near a solid boundary are examined utilizing three different thermodynamic
185 models (barotropic, non isothermal HEM and Helmholtz EoS). The most important
186 conclusions are summarised in section 4. Finally, in the Appendix section, the methodology
187 for deriving the exact solution for an arbitrary EoS where pressure is a function of both
188 density and internal energy is discussed. This methodology was used to obtain the exact

189　solution for the benchmark Riemann problem; however it may be applied in general for any
190　applicable EoS.
191
192　**2. Numerical Method**
193
194　　　Since bubble growth and collapse is an inertial phenomenon, the viscosity and surface
195　tension are neglected in the present study (Zhang et al., 1993). The 2D Euler equations in *r-z*
196　cylindrical coordinates with a geometric source term in order to take into account cylindrical
197　symmetry (Toro, 2009) are:
198
199　$\mathbf{U}_t + \mathbf{F(U)}_r + \mathbf{G(U)}_z = \mathbf{S(U)}, in\ \Omega$　　　　　　　　　　　　(1)
200
201　where *t, r, z* subscripts indicate differentiation with respect to time, *r* direction and *z* direction
202　respectively. $\mathbf{U}$ is the conserved variable vector, $\mathbf{F(U)}$ and $\mathbf{G(U)}$ are the fluxes at the radial (*r*)
203　and axial (*z*) directions respectively and $\mathbf{S(U)}$ is the geometric source term, to take into
204　account axial symmetry. Ω represents the volume of the computational domain, while $\partial\Omega$ the
205　boundary of the domain. The vectors of eq. 1 are:
206

207　$\mathbf{U} = \begin{bmatrix} \rho \\ \rho u_r \\ \rho u_z \\ \rho E \end{bmatrix}, \mathbf{F(U)} = \begin{bmatrix} \rho u_r \\ \rho u_r^2 + p \\ \rho u_r u_z \\ (\rho E + p)u_r \end{bmatrix}, \mathbf{G(U)} = \begin{bmatrix} \rho u_z \\ \rho u_r u_z \\ \rho u_z^2 + p \\ (\rho E + p)u_z \end{bmatrix}, \mathbf{S(U)} = -\frac{s}{r}\begin{bmatrix} \rho u_r \\ \rho u_r^2 \\ \rho u_r u_z \\ u_r(\rho E + p) \end{bmatrix}$　　(2)

208
209　where ρ is the fluid density, u_r and u_z the radial and axial velocity components respectively, *p*
210　is the pressure, *E* is the total internal energy, equal to $\frac{1}{2}\left(u_r^2 + u_z^2\right) + e$, *e* is the internal energy
211　of the fluid and *s* is the geometric source term. For cylindrical symmetry, *s* is equal to unity.
212　　　The following initial and boundary conditions are used for the PDE system:
213
214　Initial condition:　　　　　　　　　　$\mathbf{U}(r, z, t = 0) = \mathbf{U}_0(r, z), in\ \Omega$　　　(3)
215　Dirichlet type boundary condition:　　　$\mathbf{U} = \mathbf{U}_D, on\ \partial\Omega_D$　　　　　　(4)
216　Neumann type boundary condition:　　　$\dfrac{\partial\mathbf{U}}{\partial\mathbf{n}} = \mathbf{U}_N, on\ \partial\Omega_N$　　　　　(5)
217
218　**2a. Helmholtz energy equation of state for n-Dodecane**
219　　　In this section, the derivation of properties of n-Dodecane from the Helmholtz energy,
220　is discussed. The Helmholtz energy is calibrated within the temperature range
221　$263.6 \le T \le 700\,K$, for maximum pressure $p_{max} = 700\,MPa$ and maximum density
222　$\rho_{max} = 771.62\,kg/m^3$ (Lemmon and Huber, 2004). Due to the violent bubble collapses to be
223　examined later on, local conditions may exceed the aforementioned limits. Thus, the
224　Helmholtz equation was applied to derive thermodynamic properties beyond the
225　aforementioned calibration; even though there is no guarantee that the calibration of
226　the Helmholtz equation is valid in this regime, the derived properties have been checked for
227　consistency (e.g. increasing density as pressure increases, for given temperature) and were
228　found to behave in a reasonable manner, i.e. no inflexion or stationary points were found,
229　indicating a monotonic behaviour of the property functions.

230   The EoS for calculating the thermodynamic properties of n-Dodecane fuel can be
231 expressed using the Helmholtz energy, having as independent variables density and
232 temperature (Lemmon and Huber, 2004):
233

234 $$a(\rho,T) = a^0(\rho,T) + a^r(\rho,T)$$ (6)

235 The above in dimensionless form becomes:
236

237 $$\frac{a(\rho,T)}{RT} = \alpha(\delta,\tau) = \alpha^0(\delta,\tau) + \alpha^r(\delta,\tau)$$ (7)

238 where $\delta = \rho/\rho_c$, $\tau = T_c/T$.

239 The dimensionless Helmholtz energy of the ideal gas can be written in the form:
240

241 $$\alpha^0 = a_1 + a_2\tau + ln\delta + (c_0 - 1)ln\tau + \sum_{k=1}^{5} c_k ln\left[1 - exp\left(-\frac{u_k\tau}{T_c}\right)\right]$$ (8)

242 where a_1, a_2 are arbitrary values set by the reference state. The residual Helmholtz energy is
243 written in the following non-dimensional form:
244

245 $$\alpha^r(\delta,\tau) = n_1\delta\tau^{0.32} + n_2\delta\tau^{1.23} + n_3\delta\tau^{1.5} + n_4\delta^2\tau^{1.4} + n_5\delta^3\tau^{0.07} + n_6\delta^7\tau^{0.8}$$
$$+ n_7\delta^2\tau^{2.16}exp^{-\delta} + n_8\delta^5\tau^{1.1}exp^{-\delta} + n_9\delta\tau^{4.1}exp^{-\delta^2} + n_{10}\delta^4\tau^{5.6}exp^{-\delta^2}$$
$$+ n_{11}\delta^3\tau^{14.5}exp^{-\delta^3} + n_{12}\delta^4\tau^{12.0}exp^{-\delta^3}$$ (9)

246   Equation 7 may be manipulated to obtain all important thermodynamic properties, like
247 pressure p, internal energy e, enthalpy h, entropy s and speed of sound c as a function of
248 density ρ and temperature T; the interested reader is addressed to (Lemmon and Huber, 2004)
249 for the manipulations needed and the coefficients of eq. 9. Saturation conditions are identified
250 using the Maxwell criterion, i.e. the pressure for which the Gibbs free energy of the liquid and
251 vapour phases are equal. Upon identifying the saturation pressure as a function of
252 temperature, the saturation dome may be identified; within the saturation dome fluid
253 properties are determined using the mixture assumption based on the volume fraction a, i.e.:
254

255
$$\rho = (1-a)\rho_{sat,L} + a\rho_{sat,V}$$
$$\rho e = (1-a)e_{sat,L}\rho_{sat,L} + ae_{sat,V}\rho_{sat,V}$$
$$\rho h = (1-a)h_{sat,L}\rho_{sat,L} + ah_{sat,V}\rho_{sat,V}$$
$$\rho s = (1-a)s_{sat,L}\rho_{sat,L} + as_{sat,V}\rho_{sat,V}$$ (10)

256 Mixture speed of sound is determined using the Wallis speed of sound formula (Brennen,
257 1995):
258

259 $$\frac{1}{\rho c^2} = \frac{1-a}{\rho_{sat,L}c_{sat,L}^2} + \frac{a}{\rho_{sat,V}c_{sat,V}^2}$$ (11)

260 In eq. 10 and 11, the sat,L index indicates the relevant property at saturation conditions for
261 liquid and sat,V for vapour.

262   The aforementioned procedure can be performed on the fly, during code execution.
263 However, in practice it requires root finding of non-linear equations, since the Helmholtz
264 equation (and consequently all derived properties) is naturally expressed as a function of

265 density ρ and temperature T, whereas the flow solver calculates density ρ and internal energy
266 e. In other words, at each time step the conservative variables $(\rho, \rho E)$ must be transformed to
267 (ρ, T) and then used to derive pressure and speed of sound for the next calculation step. This
268 can be done, using e.g. the Newton Raphson method, however it is very time consuming and
269 inefficient.

270   Instead of solving the aforementioned EoS for each time step (using for example the
271 Newton-Raphson method or similar), a similar technique as the one employed by Dumbser et
272 al. (2013) has been used. In the present work, an unstructured thermodynamic table has been
273 used (instead of the Cartesian used in Dumbser's work et al. (2013)), constructed prior to the
274 simulations andcontaining the thermodynamic properties derived from the Helmholtz EoS.
275 Static linked lists have been used in order to split the thermodynamic table into smaller
276 groups of data and search only the group that has the desired values within its range. The
277 resulting algorithm is much more efficient than the on-the-fly calculation of the Helmholtz
278 EoS, by almost one order of magnitude of the computational time.

279   The unstructured thermodynamic table is built by selecting an appropriate range for the
280 density and the internal energy: $\rho_{min} \leq \rho \leq \rho_{max}$ and $e_{min} \leq e \leq e_{max}$ that define a 2-D table
281 $\Sigma = [\rho_{min}, \rho_{max}] \times [e_{min}, e_{max}]$, which should enclose the expected conditions of the simulation.
282 Then this table Σ is discretized with quadrilateral elements. An unstructured grid of
283 approximately 40,000 elements was created (Figure 1). The grid was refined around the
284 saturation line in order to accurately capture the large variation of the thermodynamic
285 properties in this area (e.g. for speed of sound or internal energy). Indicatively, the three
286 dimensional phase diagram derived from the above Helmholtz energy EoS for the n-
287 Dodecane, expressing pressure, internal energy and speed of sound as a function of density
288 and temperature, is shown in Figure 2.

289   During the algorithm execution, after calculating the conservative vector in the time
290 loop, and hence the density and the internal energy are known, the element of the
291 thermodynamic table in which each cell of the computational domain belongs may be
292 determined, using the linked list algorithm. Then using a Finite Element bilinear interpolation,
293 any thermodynamic property φ in the space Σ can be calculated as:

294

295 $$\varphi(\rho, e) = \sum_{n}^{nodes} N_n(\rho, e) b_n \tag{12}$$

296 where φ can either be pressure, temperature or speed of sound, which are needed for the
297 calculation of the fluxes (see section 2d) or post-processing results. The unknown coefficients
298 of φ are notated by b and N is the shape function of node n:

299

300 $$N_n(\rho, e) = 1 + (e - e_n) + (\rho - \rho_n) + (e - e_n)(\rho - \rho_n) \tag{13}$$

301 The b coefficients of the property φ for each element are calculated by solving the following
302 equation:

303

304 $$[N]\mathbf{b} = \varphi \rightarrow \begin{bmatrix} N_{11} & N_{12} & N_{13} & N_{14} \\ N_{21} & N_{22} & N_{23} & N_{24} \\ N_{31} & N_{32} & N_{33} & N_{34} \\ N_{41} & N_{42} & N_{43} & N_{44} \end{bmatrix} \begin{bmatrix} b_1 \\ b_2 \\ b_3 \\ b_4 \end{bmatrix} = \begin{bmatrix} \varphi_1 \\ \varphi_2 \\ \varphi_3 \\ \varphi_4 \end{bmatrix} \tag{14}$$

305 where φ are the values of the property at the nodes of the quadrilateral element and N_{mn} is:

306

307 $$N_{mn} = 1 + (e_m - e_n) + (\rho_m - \rho_n) + (e_m - e_n)(\rho_m - \rho_n)$$ (15)

308 The most efficient way to find the coefficients b, is to calculate in advance and store the
309 inverse of the mass matrix [N] for all elements before time advancement begins. That way,
310 the coefficients b for each property φ can be found:

311 $$\mathbf{b} = [\mathrm{N}]^{-1}\varphi$$ (16)

312 After finding the conservative vector in the time loop, each thermodynamic property φ can be
313 approximated from equation (12).
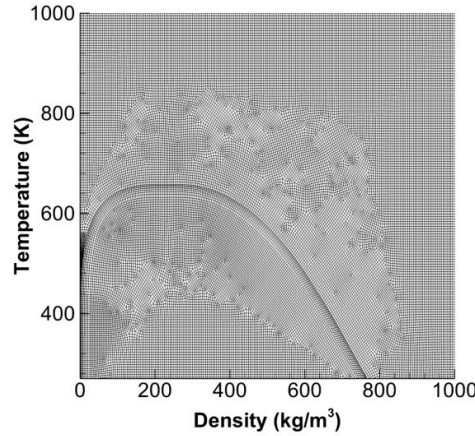
314
315 **Figure 1:** Unstructured thermodynamic grid of 40,000 finite elements, refined near the saturation line.
316

317
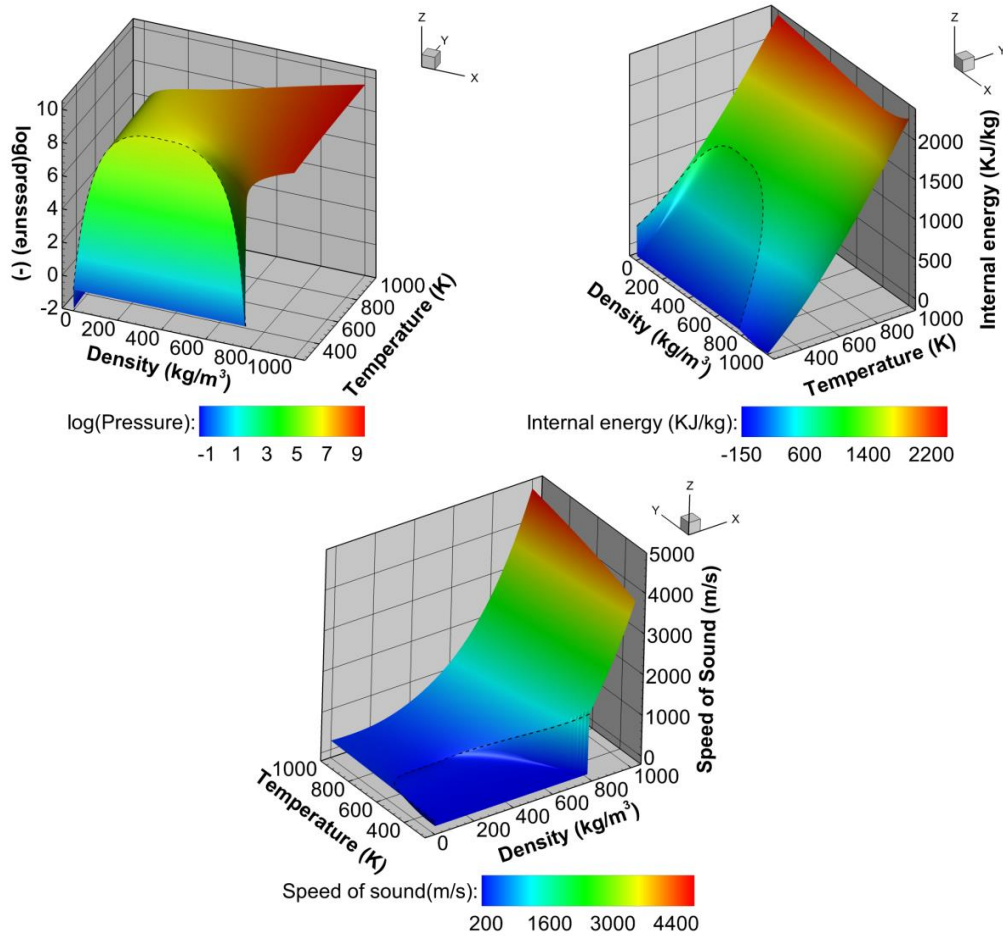
318
319 **Figure 2:** Three dimensional phase diagrams for the n-Dodecane, where the dashed line is the
320 saturation line. The properties have been derived from the Helmholtz energy EoS.

8

2b. Barotropic approach

A two-step barotropic equation of state, which has been validated and used in previous studies (Koukouvinis et al., 2016a), has been used for comparison with the Helmholtz equation of state. In the former, the modified Tait equation of state for the liquid part and an isentropic-resembling relation (Egerer et al., 2014) for the mixture are given:

$$p(\rho) = \begin{cases} B\left[\left(\dfrac{\rho}{\rho_{sat,L}}\right)^n - 1\right] + p_{sat}, & \rho \geq \rho_{sat,L} \\[4mm] p_{sat} + C\left(\dfrac{1}{\rho_{sat,L}} - \dfrac{1}{\rho}\right), & \rho < \rho_{sat,L} \end{cases} \tag{17}$$

In this approach, the saturation properties have been calculated assuming constant temperature at 300 K. The energy equation is not solved and thus, after solving the continuity and momentum equations, the above formula is used for calculating the pressure. This method is robust and efficient but it lacks in the prediction of the temperature field.

2c. Homogeneous equilibrium mixture with temperature effects

Finally, the third thermodynamic model which has been utilized, is a more sophisticated extension of the previous barotropic model, since the saturation properties depend on temperature (Koop, 2008; Schmidt et al., 2006). In this case, the modified Tait equation is used for the liquid, the ideal gas EoS for the vapour and the Wallis formula for the mixture. This model is based on the assumption that the latent heat is constant and it is calculated based on the initial temperature $T_0=300\ K$, which is valid only for a small variation of the temperature. Moreover, it cannot predict transcritical to supercritical transitions. The pressure is given by the following three-step equation as a function of density and temperature:

$$p(\rho,T) = \begin{cases} B\left[\left(\rho/\rho_{sat,L}(T)\right)^n - 1\right] + p_{sat}(T), & \rho \geq \rho_{sat,L}(T) \\ p_{sat}(T), & \rho_{sat,V}(T) < \rho < \rho_{sat,L}(T) \\ \rho R T, & \rho < \rho_{sat,V}(T) \end{cases} \tag{18}$$

and the internal energy is given by the following equation:

$$e(T) = \begin{cases} C_{vl}(T-T_0) + e_{l0}, & \rho \geq \rho_{sat,L}(T) \\ \left(\alpha\rho_{sat,V}(T)e_{vap}(T) + (1-\alpha)\rho_{sat,L}(T)e_{liq}(T)\right)/\rho, & \rho_{sat,V}(T) < \rho < \rho_{sat,L}(T) \\ C_{vv}(T-T_0) + L_v(T_0) + e_{l0}, & \rho < \rho_{sat,V}(T) \end{cases} \tag{19}$$

where e_{vap} and e_{liq} stand for the internal energy of the vapour and liquid from the third or the first step of the equation respectively. After calculating the solution vector and thus the total energy is known, the Newton-Raphson method has been employed for the following function in order to calculate the temperature:

$$F(T) = e(T) - E(T) + \frac{1}{2}\left(u^2 + v^2\right) = 0 \tag{20}$$

Once the Newton-Raphson algorithm has converged, the pressure and the volume fraction are calculated and then the algorithm advances to the next time step.

For each Newton-Raphson iteration, the saturation properties are calculated since they depend on the temperature and they are given by the following formulas:

355

$$ln\left(\frac{p_{sat}(T)}{p_c}\right) = \frac{T_c}{T}\sum_{i=1}^{7}\alpha_i\theta^{\hat{\alpha}_i} \tag{21}$$

356

$$\frac{\rho_{sat,L}(T)}{\rho_c} = \sum_{i=1}^{7}b_i\theta^{\hat{b}_i} \tag{22}$$

357

$$ln\left(\frac{\rho_{sat,V}(T)}{\rho_c}\right) = \sum_{i=1}^{7}c_i\theta^{\hat{c}_i} \tag{23}$$

358

359 where $\theta = T/T_c$ and the coefficients are given in Table 1 and $\rho_c=226.55\ kg/m^3$, $p_c=1817000$
360 Pa, $\gamma=1.03$. It must be mentioned here that the previous equations are valid as long as the
361 temperature is within the range: $T \in [T_r = 273.15, T_c = 658.1]$. The coefficients in equations
362 21-23 have been calculated in order to give the same saturation conditions as the Helmholtz
363 energy EoS.

364

365   **Table 1:** Parameters needed in Equations 19, 20 and 21 for the n-Dodecane.

Index	a_i	$\hat{a}_i$	b_i	$\hat{b}_i$	c_i	$\hat{c}_i$
1	-0.03359	0	1.37610	0	-0.39275	0
2	-8.54218	1	11.88513	1	-19.73929	1
3	3.20579	3	-69.63935	2	78.72869	2
4	11.27780	4	297.58733	3	-361.4296	3
5	7.66350	5	-717.4947	4	779.84876	4
6	-7.09773	6	888.91121	5	-899.4366	5
7	0	0	-438.5464	6	331.66738	6

366

367 This method is efficient but not so robust as the barotropic model and it suffers from
368 limitations in the temperature range relative to the Helmholtz EoS.

369

370 **2d. Space and time discretization**

371   In cavitation phenomena there is large variation in the speed of sound and thus in the
372 Mach number, making it difficult to apply a unified discretization method. The flow can be
373 considered incompressible in the liquid regime and the Mach number can even be of the order
374 of 10^{-2}. On the other hand, in the vapour regime and during the collapse of the cavity
375 structures where shock waves are created, the flow is highly compressible and Mach number
376 can be of the order of 10^2 or even higher, due to the small speed of sound of the two-phase
377 mixture (Van der Heul et al., 2000). When using density-based solvers for low Mach number
378 flows, slow convergence and incorrect solutions have been noticed (Guillard and Viozat,
379 1999; Meister, 1999; Munz et al., 2003). To overcome this, the Mach consistent numerical
380 flux of Schmidt et al. (2008) has been implemented, which is based on the HLLC flux and the
381 AUSM flux (Meng-Sing, 2006). The numerical flux in the x direction at the i+1/2 interface
382 takes the following form:

383
$$\mathbf{F}_{i+1/2}^{hybrid} = \rho_{L/R}u_{face}\begin{pmatrix} 1 \\ u_{L/R} \\ v_{L/R} \\ E_{L/R} \end{pmatrix} + p_{face}\begin{pmatrix} 0 \\ 1 \\ 0 \\ u_{face} \end{pmatrix} \tag{24}$$

384 where

385
$$u_{face} = \frac{1}{\rho_L + \rho_R}\left(\rho_L u_L + \rho_R u_R + \frac{p_L - p_R}{c_{face}}\right), \ p_{face} = \frac{p_L + p_R}{2}, \ c_{face} = max(c_L, c_R) \tag{25}$$

386 and $\rho_{L/R}$, $u_{L/R}$, $v_{L/R}$ and $E_{L/R}$ depend on the sign of u_{face}, the value of the left cell is taken when
387 the sign of u_{face} is positive and vice versa. In order to achieve 2nd order of accuracy in space,
388 the MUSCL-Hancock (Toro, 2009) reconstruction is employed to determine conservative
389 variables at cell interfaces, which in turn are used for the flux estimation (eq. 24).
390 Since the cavitation phenomena which are simulated are unsteady, a four stage Runge-Kutta
391 (RK) method, 2nd order in time has been implemented. Let an initial value problem be defined
392 by the following differential equation and its initial condition:

393
$$\frac{\partial \mathbf{U}}{\partial t} = \mathbf{R}(t, \mathbf{U}), \ \mathbf{U}(t_0) = \mathbf{U}_0 \tag{26}$$

394 The numerical solution of this differential equation is given by the following steps, where the
395 coefficients were chosen in order to improve stability (Schmidt, 2005):

396

397
$$\mathbf{U}^1 = \mathbf{U}^n + 0.11\mathbf{R}(\mathbf{U}^n) \tag{27}$$

398
$$\mathbf{U}^2 = \mathbf{U}^n + 0.2766\mathbf{R}(\mathbf{U}^1) \tag{28}$$

399
$$\mathbf{U}^3 = \mathbf{U}^n + 0.5\mathbf{R}(\mathbf{U}^2) \tag{29}$$

400
$$\mathbf{U}^{n+1} = \mathbf{U}^n + \mathbf{R}(\mathbf{U}^3) \tag{30}$$

401 This specific RK method was selected since it has low storage requirements and only the
402 solution vectors from time n and n+1 need to be stored, which is important for large scale
403 simulations.

404

405 **3. Results**

406   In this section, the numerical model is firstly validated against the exact solution of the
407 Riemann problem and the Rayleigh collapse test case and then a numerical experiment of
408 bubble collapse is performed. The Riemann problem was chosen in order to validate the
409 spatial accuracy of the algorithm and to examine if it is feasible to capture the correct wave
410 pattern. On the other hand, the Rayleigh collapse test case was chosen to investigate the time
411 advancement of the Runge-Kutta implementation, as well as the source terms. Once the
412 algorithm is validated with these cases that exact or semi-analytical solutions exist, bubble
413 collapse simulations in the vicinity of a wall have been performed for various configurations.
414 It has to be mentioned here that although in the literature many bubble collapse simulations
415 have been made, there has not been an investigation on the effect of accurate thermodynamics
416 of the fluid involved. Therefore, the present model is accessed against the barotropic model
417 and the HEM with temperature effects.

418

419 **3a. Riemann problem**

420   The first benchmark case is the Riemann problem in the computational domain
421 $x \in [-2,2]$ with initial conditions for the left state: ρ_L=752.5 kg/m^3, T_L=289 K and for the
422 right state: ρ_R=717.5 kg/m^3, T_R=350 K. Comparison between the exact and the numerical
423 solution is shown in Figure 3 at time t=0.5 μs. First order of spatial accuracy with 800 equally
424 spaced cells in the x direction was used. Wave transmissive boundary conditions have been
425 used for the left and the right side of the shock tube, that is $\mathbf{U}^{n+1}(x=L)=\mathbf{U}^n(x=L)$ and
426 $\mathbf{U}^{n+1}(x=0)=\mathbf{U}^n(x=0)$. As it can be seen in Figure 3, the exact solution of the Riemann problem

and the computed one are in satisfactory agreement and the wave pattern has been correctly
captured. The exact solution of the Riemann problem is not trivial for an arbitrary EoS and it
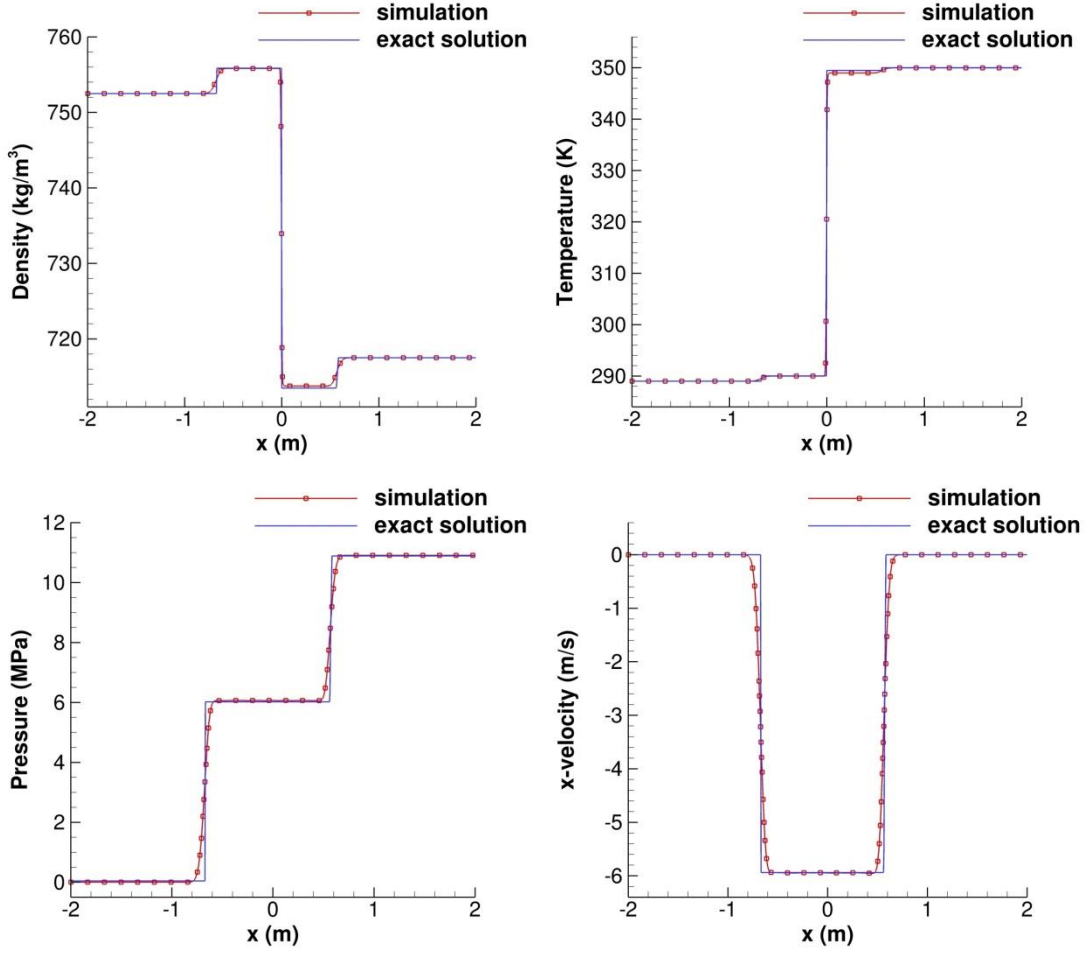has been derived following the Appendix section of the present paper.

Figure 3: Validation of the solver in the Riemann problem. Comparison of the density (upper left), temperature (upper right), pressure (lower left) and x-velocity (lower right) between the exact and the numerical solution.

3b. Rayleigh bubble collapse

The second test case examined is the Rayleigh bubble collapse, where a vapour sphere of radius $R = 400\,\mu$m is under compression owing to the higher pressure of the surrounding liquid. The bubble collapse velocity is given by Franc and Michel (2005):

$$\frac{dR}{dt} = -\sqrt{\frac{2}{3}\frac{p_\infty - p_{vap}}{\rho_{liq}}\left[\left(\frac{R_0}{R}\right)^3 - 1\right]} \tag{31}$$

and the characteristic Rayleigh time τ of the bubble is:

$$\tau = 0.915 R_0 \sqrt{\frac{\rho_{liq}}{p_\infty - p_{vap}}} \tag{32}$$

Here, the vapour pressure is $p_{vap} = 19.64\,Pa$, the liquid density is $\rho_{liq} = 744.36\,kg/m^3$ and the far-field pressure is $p_\infty = 0.1\,MPa$.

447   An one-dimensional solver was employed for this simulation, taking advantage of the
448   spherical symmetry. The total computational domain is 20 times the size of the initial vapour
449   radius in order to minimize the interference of the boundaries. The mesh is refined in the
450   bubble region, where 1000 equally spaced cells have been used and a stretching ratio of 1.05
451   with 150 cells has been used outside the bubble. Wave transmissive boundary condition has
452   been used on the far-field right side and symmetry condition was selected for the left side.
453   Comparison with the semi-analytical solution gives satisfactory results (Figure 4), since the
454   current methodology is able to predict the correct curve of the bubble radius with respect to
455   time. In Figure 4, the radius has been divided by the initial radius R_0 and the time has been
456   non-dimensionalized by the Rayleigh time which is $\tau=31.5 \ \mu s$ for the current configuration.
457
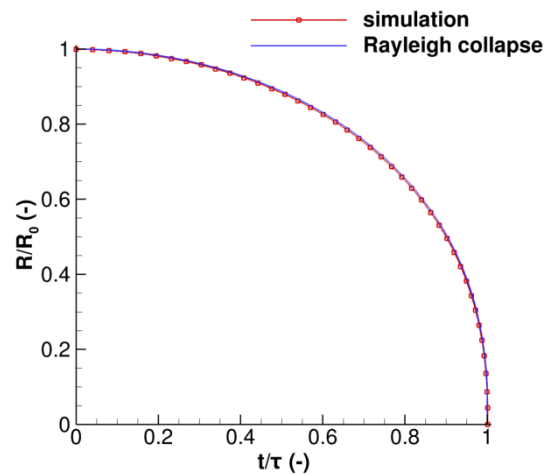
459   **Figure 4:** Comparison between the Rayleigh collapse solution and the numerical one. The bubble
460   radius and the time are expressed in non-dimensional form, in reference to the initial radius R_0 and
461   Rayleigh collapse time τ respectively.
462

3c. n-Dodecane bubble collapse

464   The collapse of a n-Dodecane vapour bubble in the vicinity of a wall has been
465   investigated next. Following Lauer et al. (2012) and Koukouvinis et al. (2016a), the same
466   configuration is tested for the numerical scheme presented in section 2, which takes into
467   account temperature effects. The radius of the bubble is $R=400 \ \mu m$ and its centre has been
468   placed at distance $d=416, \ 140$ and $-140 \ \mu m$ from the horizontal wall (x-axis) and on the axis
469   of symmetry (y-axis), as it can be seen in Figure 5. The properties of the n-Dodecane in liquid
470   form which is surrounding the bubble are $p_l=12.144 \ MPa$, $T_l \approx 300 \ K$ and the vapour bubble
471   properties are $p_v=19.64 \ Pa$, $T_v \approx 300 \ K$. The computational domain is 20 times the bubble
472   radius; 200 equally spaced cells were used for describing the initial radius of the bubble. After
473   distance 2.5R from the origin, the mesh is coarsened with ratio 1.05 in both directions. Zero
474   gradient boundary condition has been used for the right and the upper side, slip wall for the
475   lower side, whereas for the y-axis of symmetry, the normal velocity component is zero.
476   In Figures 6, 7 and 8 there are two columns of images. In the first column the pressure
477   field is shown on the left and the velocity field on the right. Similarly, in the second column
478   the temperature field is shown on the left and Schlieren is depicted on the right. In all images,
479   iso-lines of density 380 kg/m³ are shown as well. In Figures 9, 10 and 11 wall pressure (left)
480   and wall temperature (right) combined with the density iso-surface of 380 kg/m³ are shown.
481   The units are in SI or their submultiples and multiples of the SI units. The simulation time

482   indicated in the next Figures is non-dimensional and it is divided by the Rayleigh collapse
483   time $\tau = 2.88\ \mu s$.
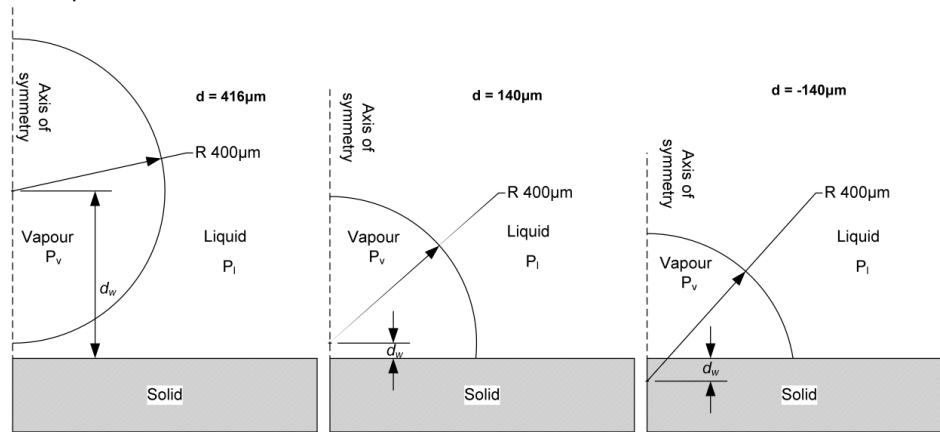

484
485   **Figure 5:** Bubble configurations for the three different positions.
486

487   In all three configurations, there is slow shrinking of the bubble initially, until the jet is
488   formed and after that the bubble is collapsing rapidly. Of course, the direction of the jet
489   depends on the configuration, as it will be explained below.
490   In Figure 6 the evolution of the bubble collapse is shown for the configuration where
491   its initial centre is placed at $d = 416\ \mu m$ from the x-axis. At the beginning of the collapse, a
492   rarefaction wave expands from the bubble. The interaction of the rarefaction wave with the
493   wall causes local depressurisation and vaporisation in the vicinity of the wall (Koukouvinis et
494   al., 2016a). As the collapse proceeds, the bubble shape departs from spherical, due to the
495   interaction with the wall boundary (x-axis). A micro-jet is formed on the top of the bubble
496   and the heart-like-shape is noticed, which is in accordance with previous results reported
497   (Koukouvinis et al., 2016a; Lauer et al., 2012). In addition, the propagating pressure wave
498   after collapse is shown at time 1.18 in Figure 6. There is a significant rise in the temperature
499   of the liquid, up to 1000 K, after the collapse of the bubble, due to vapor condensation and
500   liquid compression, while there is a significant drop in the temperature above the bubble, to
501   273 K, due to the large acceleration of the flow which causes a reduction in the internal
502   energy. We highlight here, that the critical point for n-dodecane is $T_c \sim 658K$ and $p_c \sim 18bar$;
503   this implies that in areas of collapse the fluid may transition to supercritical state.
504   In Figure 7 instances of the bubble having initially its centre at $d = 140\ \mu m$ from the x-
505   axis are shown. Again, a non-symmetric shape for the bubble and a micro-jet are created. A
506   torus which is attached to the wall is formed and it collapses creating a pressure wave. In both
507   cases, that is for $d = 416\ \mu m$ and $d = 140\ \mu m$, the jet's and the bubble collapse direction are
508   towards the wall. In this specific case, a secondary jet is created when the primary jet, which
509   is normal to the wall, is deflected at the wall and interacts with the remaining ring (time=1.09
510   in Figure 7).
511   In Figure 8 snapshots of the bubble having its centre in the lowest position ($d = -140$
512   μm) are demonstrated. In comparison with the two previous positions, the shape of the bubble
513   looks like a pin and the collapse direction is tangential to the wall. The jet which is formed is
514   towards to the axis of symmetry, which was not the case in the previous positions. A
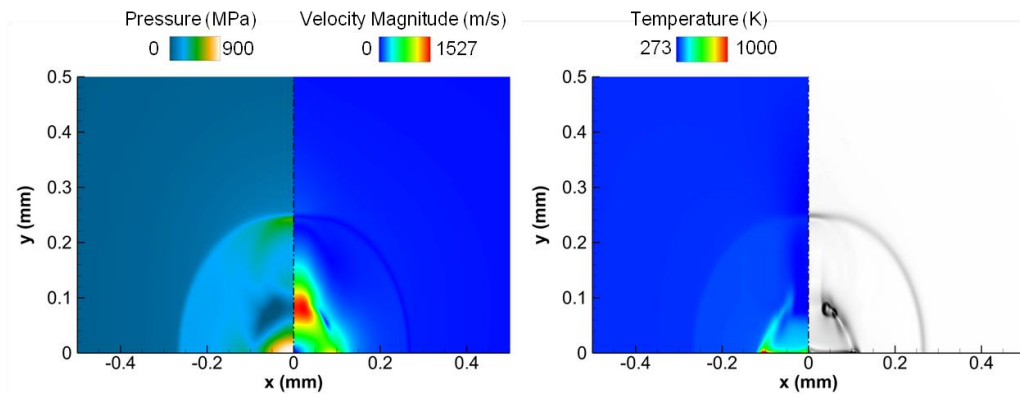515   propagating pressure wave at time 0.77 is shown in Figure 8.

516

517

518
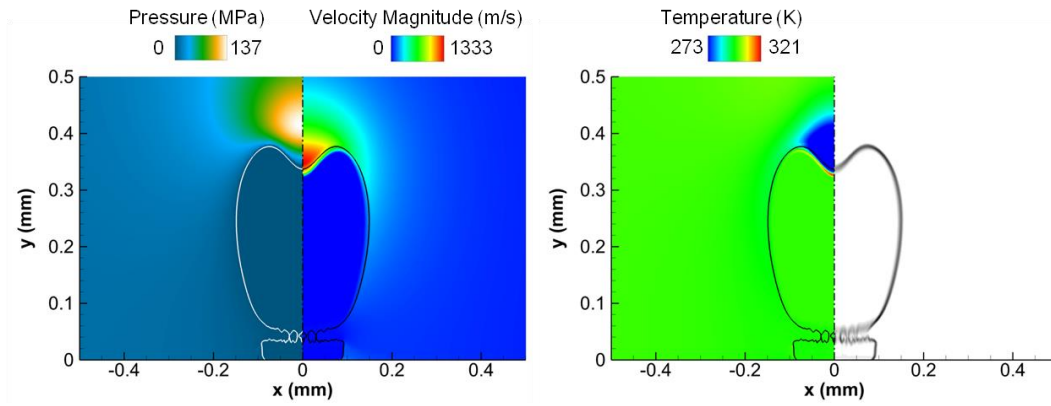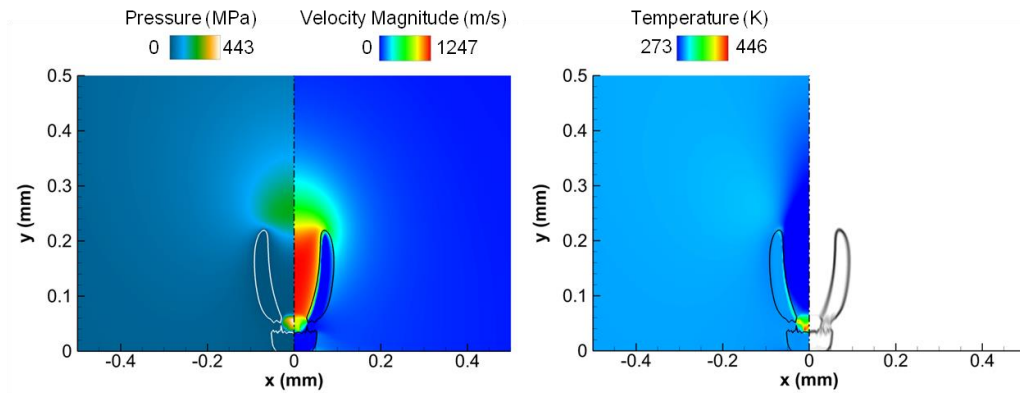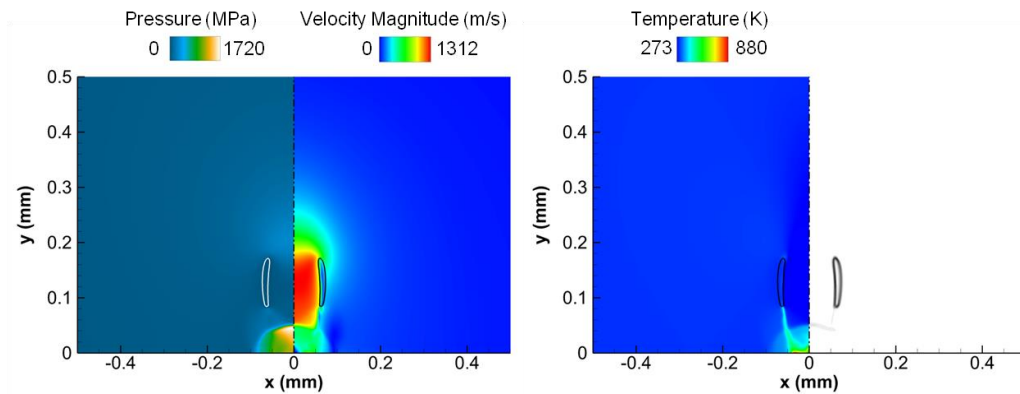
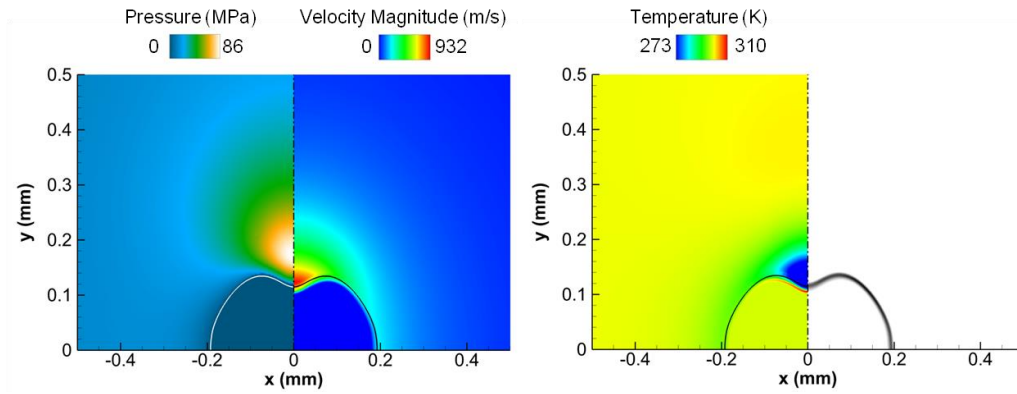519
520 **Figure 6:** Instances during the vapour bubble collapse for d=416 μm. Time has been non-
521   dimensionalized with Rayleigh collapse time τ=2.88 μs.
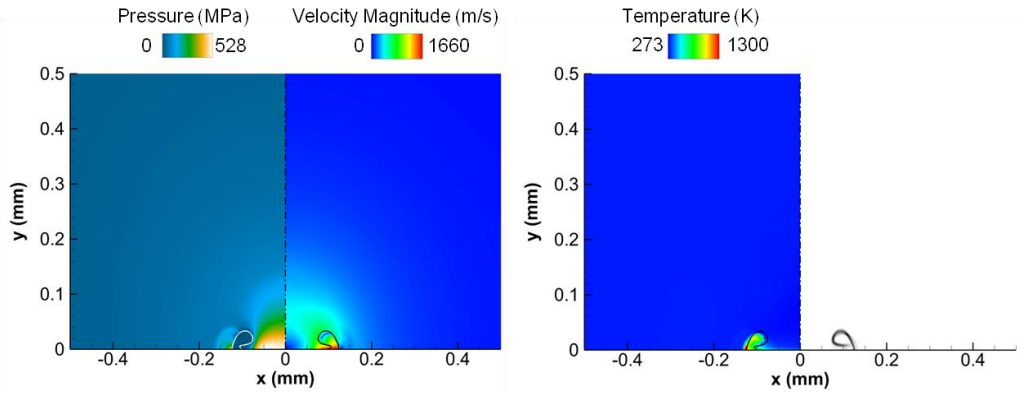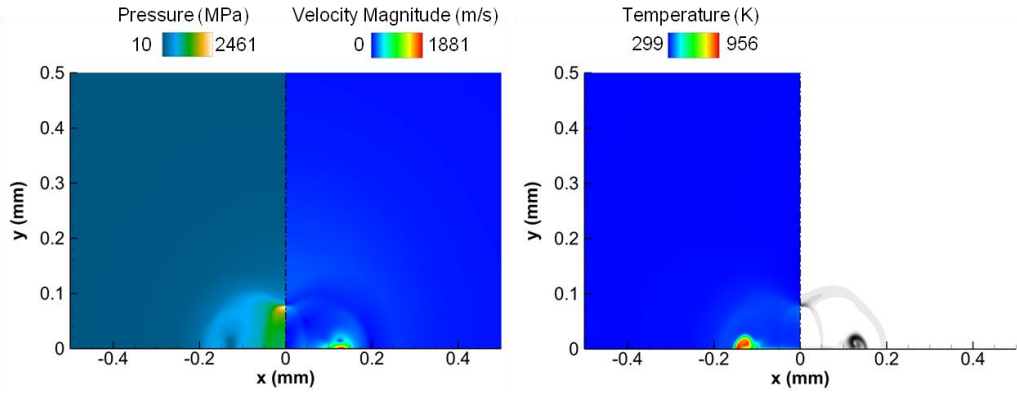
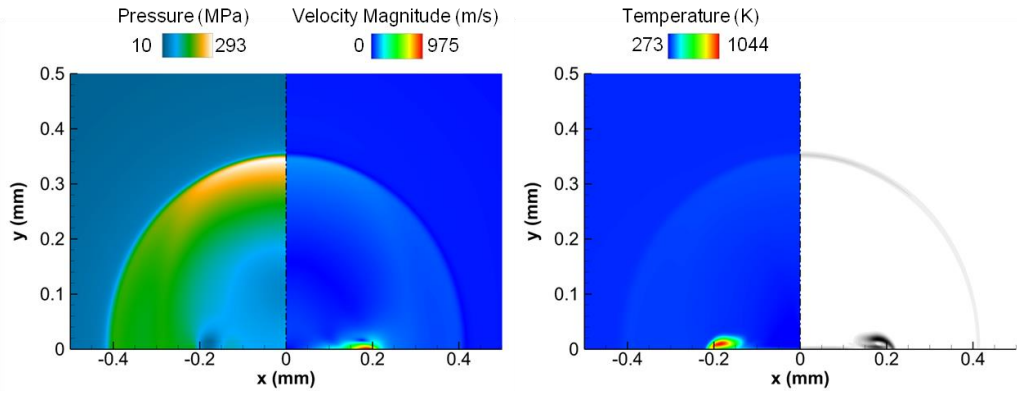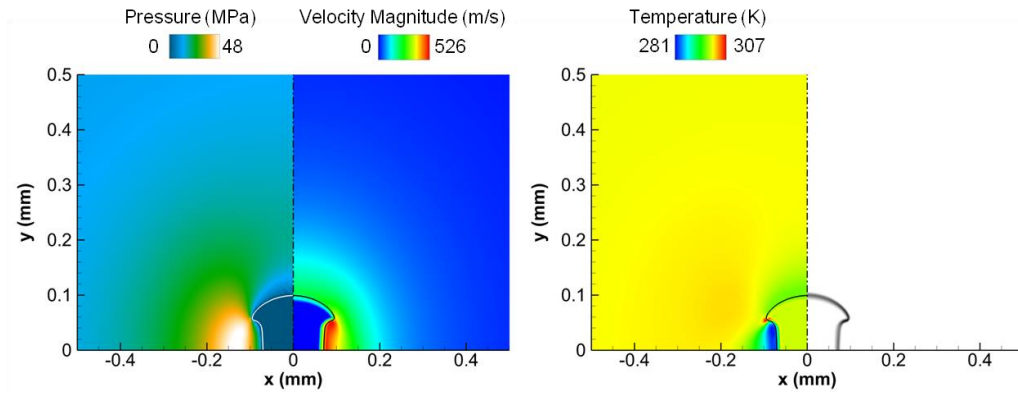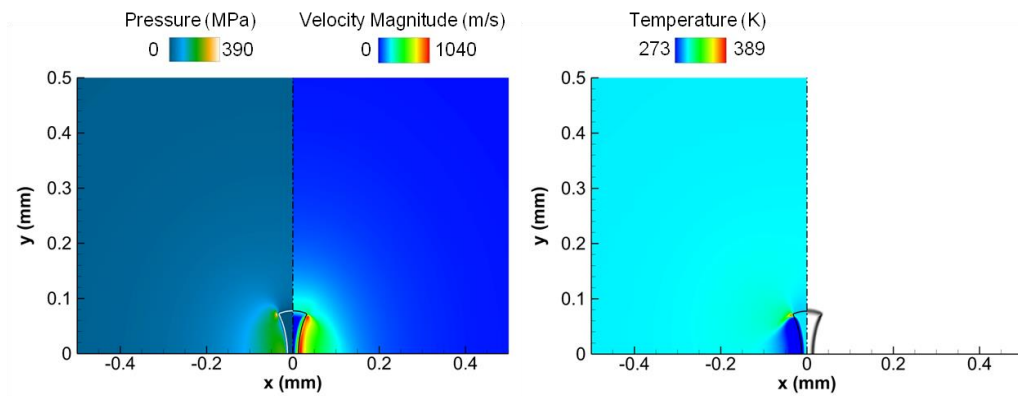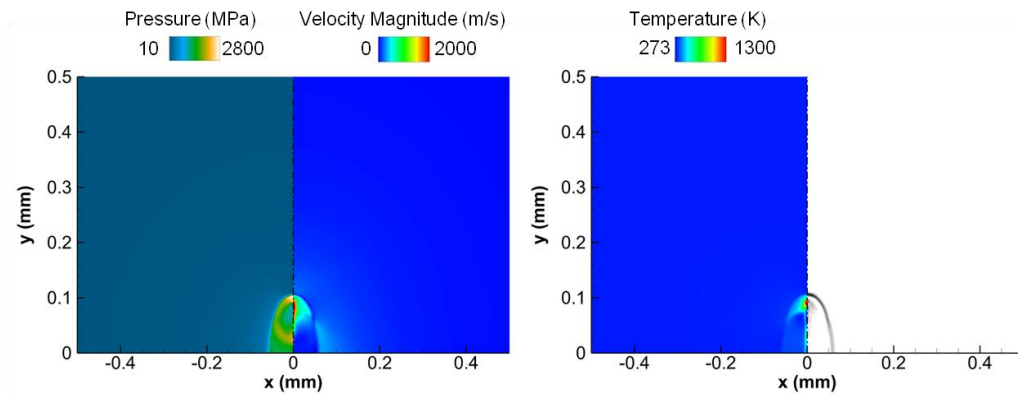**Figure 7:** Instances during the vapour bubble collapse for d=140 µm. Time has been non-dimensionalized with Rayleigh collapse time τ=2.88 µs.
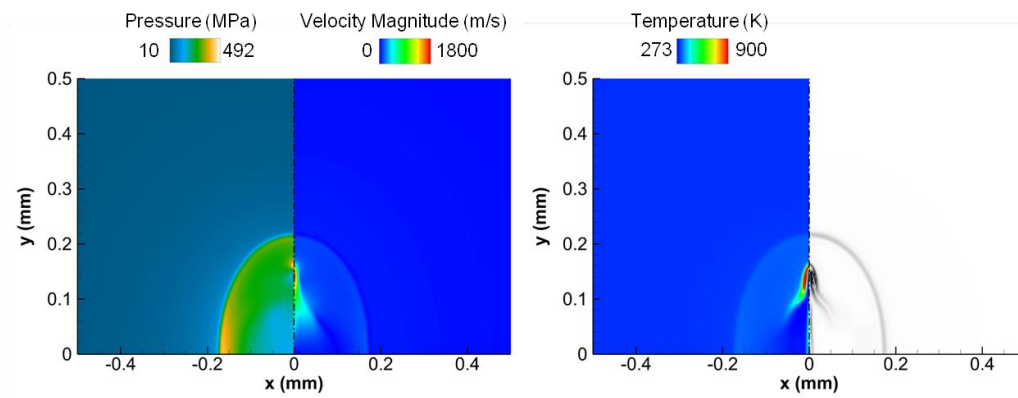
528

529

530

531

Figure 8: Instances during the vapour bubble collapse for d=-140 μm. Time has been non-dimensionalized with Rayleigh collapse time τ=2.88 μs.

532

533

534   Focusing on the iso-surfaces of Figures 9, 10 and 11, the different collapse pattern is
535 clearly visible. The justification for the collapse shape is related to the local angle between the
536 liquid/vapour interface and wall, at the closest point or point of contact to the wall; this has
537 been discussed in more detail in (Koukouvinis et al., 2016a), but the main mechanism will be
538 briefly discussed here as well. When the local angle is below 90°, flow in the vicinity of the
539 wall tends to detach, reducing the pressure and preventing further acceleration of the collapse,
540 thus near wall velocities are small and the collapse is mainly directed in the form of a micro-
541 jet towards the wall on the axis-of-symmetry. On the other hand, when the local angle is
542 higher than 90° the flow tends to move towards the wall, leading to pressurization and further
543 acceleration of the collapse. These effects underline the influence of boundary presence and
544 pressure gradients to the bubble collapse, as demonstrated also in experimental (Obreschkow
545 et al., 2006; Obreschkow et al., 2013) and numerical work (Hawker and Ventikos, 2009;
546 Lauer et al., 2012; Plesset and Chapman, 1971).

547   The collapse time of the bubbles is reasonable and comparable to the Rayleigh collapse
548 time. In the previous configurations the collapse time is also proportional to the initial volume
549 of the vapour which exists in the bubble. A more thorough study of the collapse times for the
550 previous configurations and other thermodynamic models is shown next, where two different
551 homogeneous equilibrium methods are implemented and compared to the above technique.
552 The model parameters and the initial conditions have been chosen accordingly to match the
553 conditions of the Helmholtz EoS bubble collapse, for consistency reasons.

554   The configuration of the barotropic model was made using the following values:
555 $B=125.956$ MPa, $p_{sat}=40$ Pa, $\rho_{sat}=744.29$ kg/m^3, $C=1100$ Pa kg/ m^3 and $n=7.15$. The initial
556 density of the liquid was set to $\rho_{liq}=753.91$ kg/m^3 and the density in the bubble was set to
557 $\rho_{liq}=74.0$ kg/m^3.

558   For the HEM model with temperature effects, the initial density of the liquid was set to
559 $\rho_{liq}=752.3$ kg/m^3, the density in the bubble was $\rho_{liq}=3.95$ kg/m^3 and the initial temperature was
560 $T_0=300$ K. In addition, $B=168.638$ MPa, $n=7.15$, $R=48.9$ J/(kg K), $C_{vl}=1823$ J/(kg K),
561 $C_{vv}=1593.3$ J/(kg K), $L_v=345739.0$ J/(kg K) and $e_{l0}=9450$ J/kg have been set.

562   In Figure 12 (left), vapour volume fraction with respect to time is shown for the three
563 different thermodynamic models. It is obvious that the barotropic model predicts slightly
564 earlier collapse time for all three positions of the bubble, because the pressure is expressed
565 only as a function of the density, and the temperature effect is not taken into account. The
566 other two models considering the temperature effects, predict the same collapse time and their
567 curves coincide for all three positions of the bubble. However, for the highest position after
568 the collapse, rebound is noticed for all three models but for the Helmholtz EoS this is more
569 dominant. This rebound is caused due to the conservation of angular momentum; even if the
570 solver employed is based on the Euler equations, the asymmetric near wall bubble collapse
571 induces vorticity. This vorticity causes centrifugal force, which prevents the total collapse and
572 disappearance of the bubble, at least until vorticity is dissipated by numerical diffusion. For
573 more information on the rebound of cavitating vortices the interested reader is addressed to
574 (Franc and Michel, 2005). In addition, if the EoS is expressed as a function of density and
575 internal energy, baroclinic torque is predicted, due to the misalignment of pressure and
576 density gradient vectors and as a result, more vorticity is generated (Pozrikidis, 2009). This is
577 the case for the Helmholtz EoS, where the rebound is more dominant than the barotropic
578 model. The HEM with temperature effects is weakly dependent on the temperature and thus,
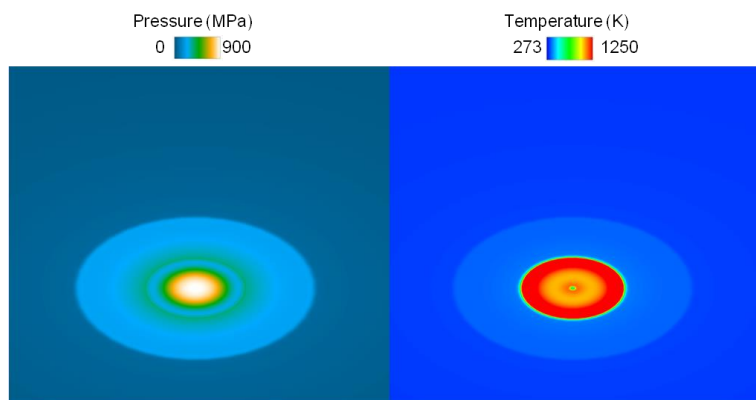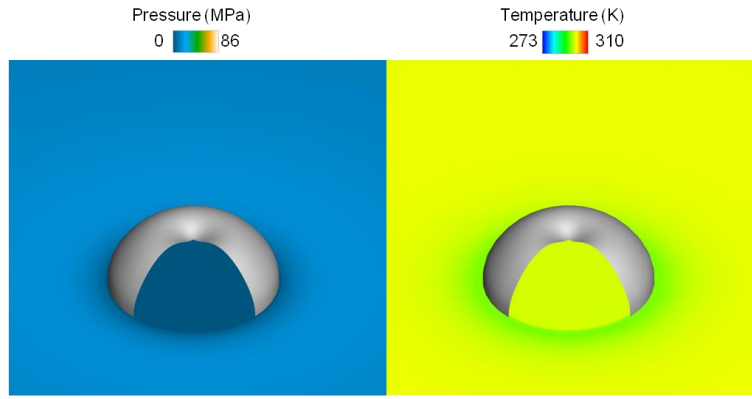579 the rebound is the same as the barotropic model.

580

581

582

583

584
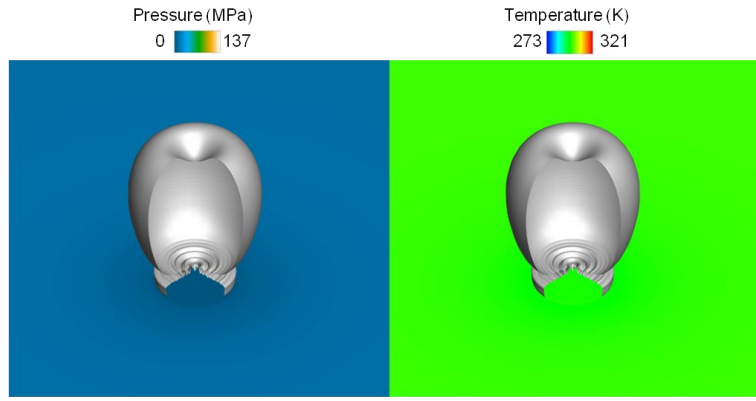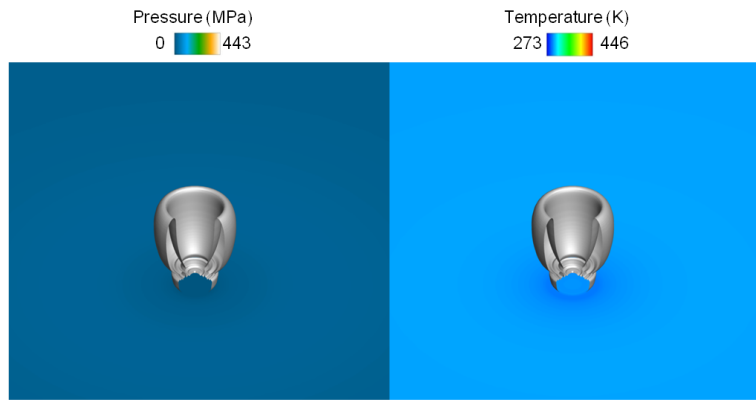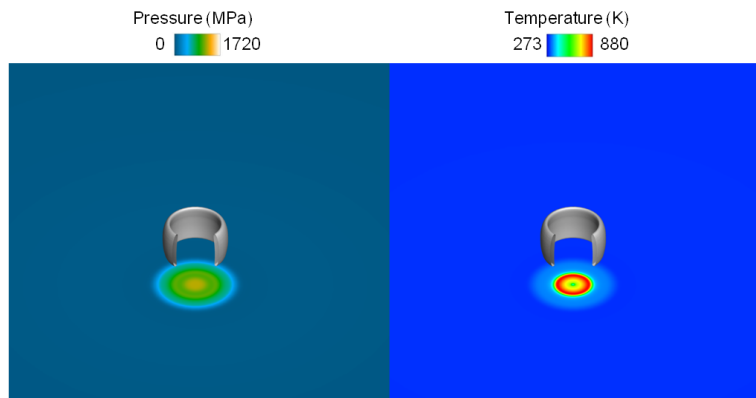
585 **Figure 9:** Wall pressure (left) and temperature (right) combined with density iso-surfaces of 380 kg/m^3
586 during the vapour bubble collapse for d=416 μm. Time has been non-dimensionalized with Rayleigh
587 collapse time τ=2.88 μs.

588

589

590
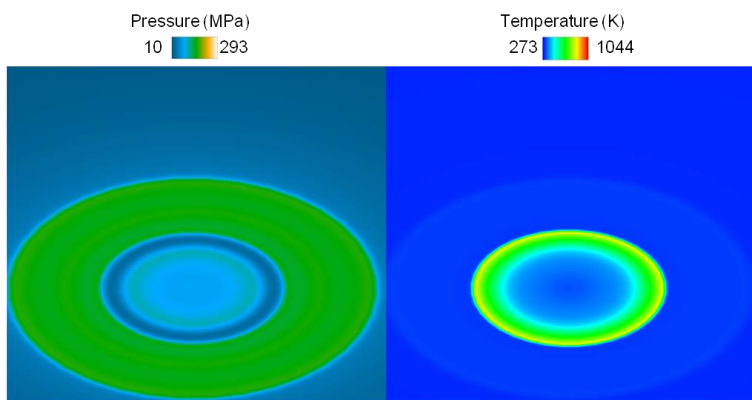
591
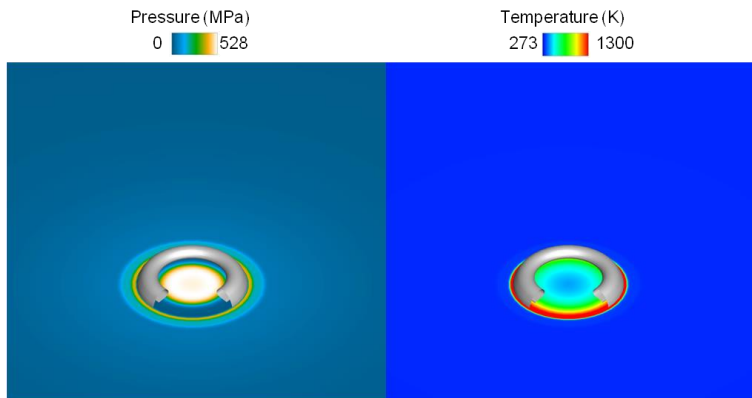592 **Figure 10:** Wall pressure (left) and temperature (right) combined with density iso-surfaces of 380
593   kg/m³ during the vapour bubble collapse for d=140 μm. Time has been non-dimensionalized with
594   Rayleigh collapse time τ=2.88 μs.
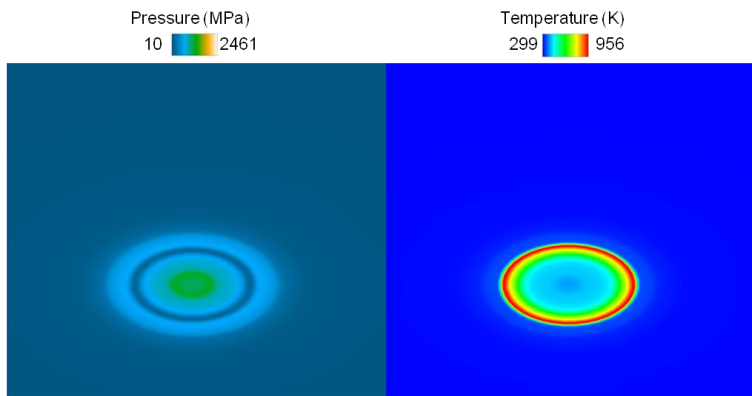
595

596

597

598
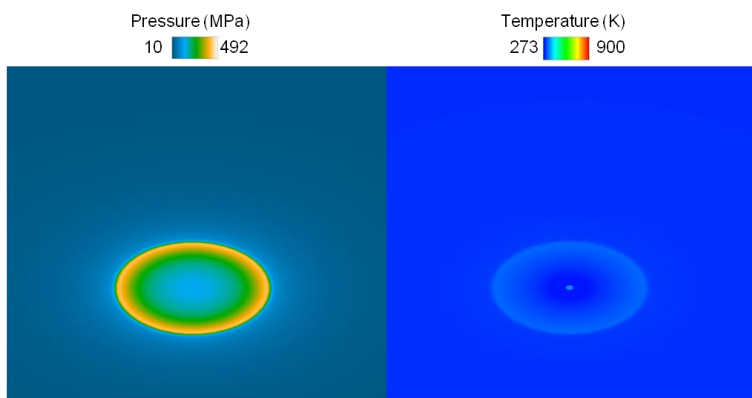
599   **Figure 11:** Wall pressure (left) and temperature (right) combined with density iso-surfaces of 380
600   kg/m^3 during the vapour bubble collapse for d=-140 μm. Time has been non-dimensionalized with
601   Rayleigh collapse time τ=2.88 μs.
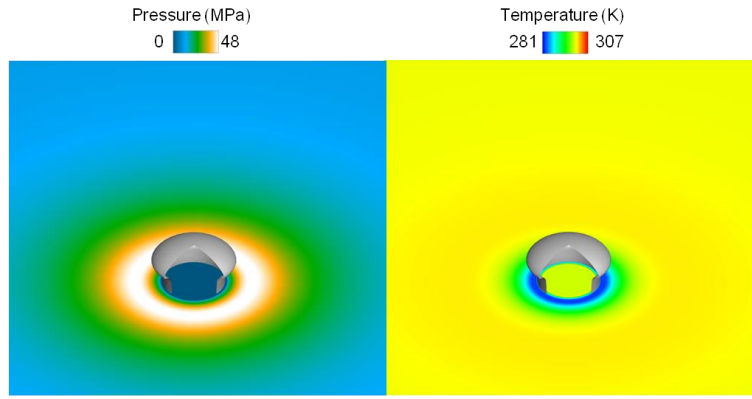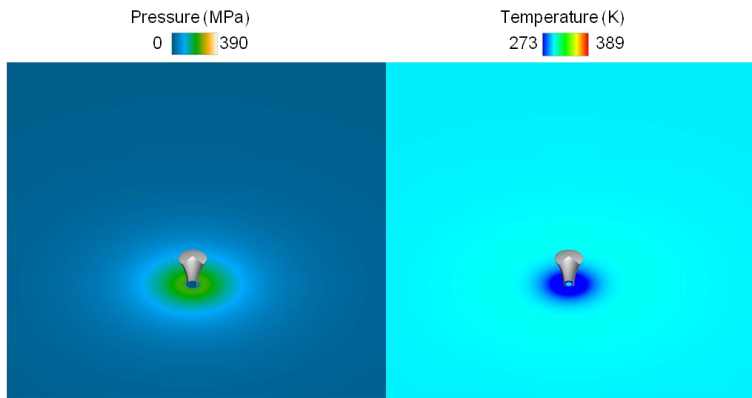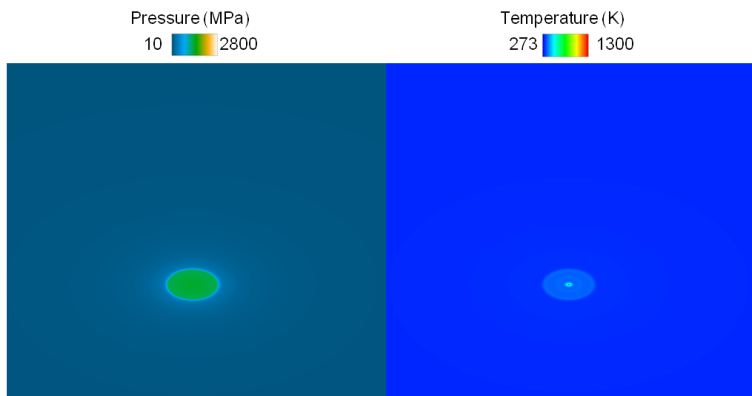
602   During the grid independence study, higher maximum pressure and temperature for the
603 finer mesh have been noticed. This is reasonable in a way that more scales can be captured
604 with the finer mesh. For example, if the vapour bubble size is smaller than the cell size, then it
605 cannot be captured with the coarse mesh and neither can the collapse. Similar observations
606 have been reached by Adams and Schmidt (2013). Furthermore, the collapse time was the
607 same, regardless the resolution of the mesh that has been used.

608   In Figure 12 (right) the maximum wall pressure is shown with respect to time, which is
609 due to the impact of the jet to the wall. It can be noticed that all the models predict similar
610 patterns for each position of the bubble and the wall pressure can even be of the order of 10^{10}
611 for the lowest position of the bubble, as it has also been shown by Koukouvinis et al. (2016a).
612 The maximum wall pressure is predicted slightly earlier in the barotropic model, as a result of
613 the earlier collapse time which was also noticed in this model. This pressure increase which is
614 due to the re-entrant jet and the shock wave after the collapse of the bubble, can lead to
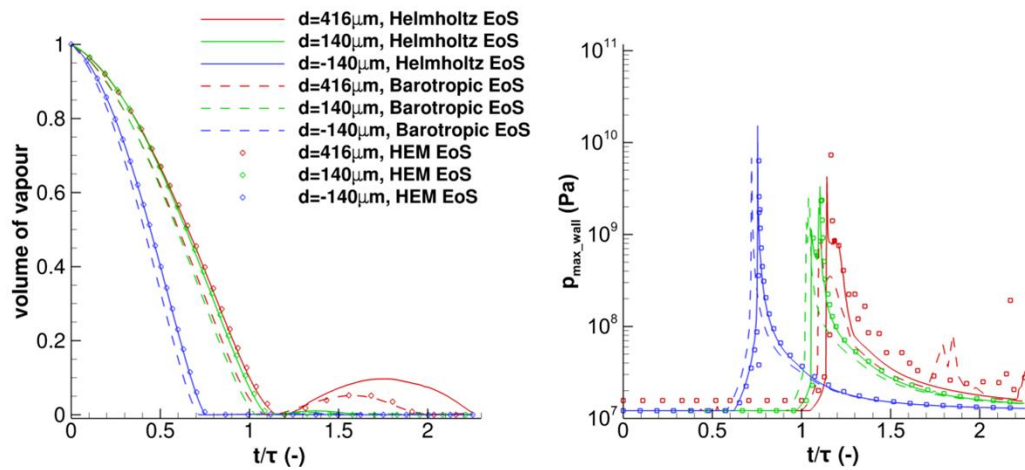615 erosion damage of materials.

616

617 **Figure 12:** Volume of vapour decrease with respect to time (left) and maximum pressure on the wall
618 (right) for the three different thermodynamic models.

619

620   In Table 2, the number of the cells where extrapolation was used beyond the
621 applicability range of the Helmholtz EoS is shown, as a percentage of the grid size. In
622 addition, the minimum and maximum values of density are also shown in order to get an
623 estimation of how extrapolation affects its value. As it can be seen, a small percentage of the
624 total cells has been calculated beyond the calibration range of the Helmholtz EoS. In Figures
625 13-15 the velocity vectors are shown and the supercritical cells (T_c=658.1 K, p_c=1.817 MPa)
626 are coloured in black, whereas the vapour (white) and liquid (grey) regions are distinguished
627 by a red iso-line of density 380 kg/m^3.

628

629   **Table 2:** Percentage of the cells where the thermodynamic properties have been calculated
630   using the Helmholtz EoS beyond its calibration limit for indicative time instances.

d=416 μm			d=140 μm			d= -140 μm		
t/τ	Cells beyond calibration	min-max ρ (kg/m^3)	t/τ	Cells beyond calibration	min-max ρ (kg/m^3)	t/τ	Cells beyond calibration	min-max ρ (kg/m^3)
1.04	1.8 %	4-826	1.01	0.5 %	4-807	0.72	0	4-777
1.13	4.2 %	3-864	1.09	0.1 %	2-890	0.75	1.2 %	4-852
1.15	3.3 %	5-994	1.10	0.1 %	553-1014	0.76	0.7 %	751-1011
1.18	1.9 %	550-916	1.14	0.9 %	388-843	0.77	0.5 %	554-868

631

632
633 **Figure 13:** Depiction of the supercritical (black), vapour (white) and liquid (grey) regions, combined
634 with velocity vectors for d=416 μm. Time has been non-dimensionalized with Rayleigh collapse time
635 τ=2.88 μs.
636

637

638
639 **Figure 14:** Depiction of the supercritical (black), vapour (white) and liquid (grey) regions, combined
640 with velocity vectors for d=140 μm. Time has been non-dimensionalized with Rayleigh collapse time
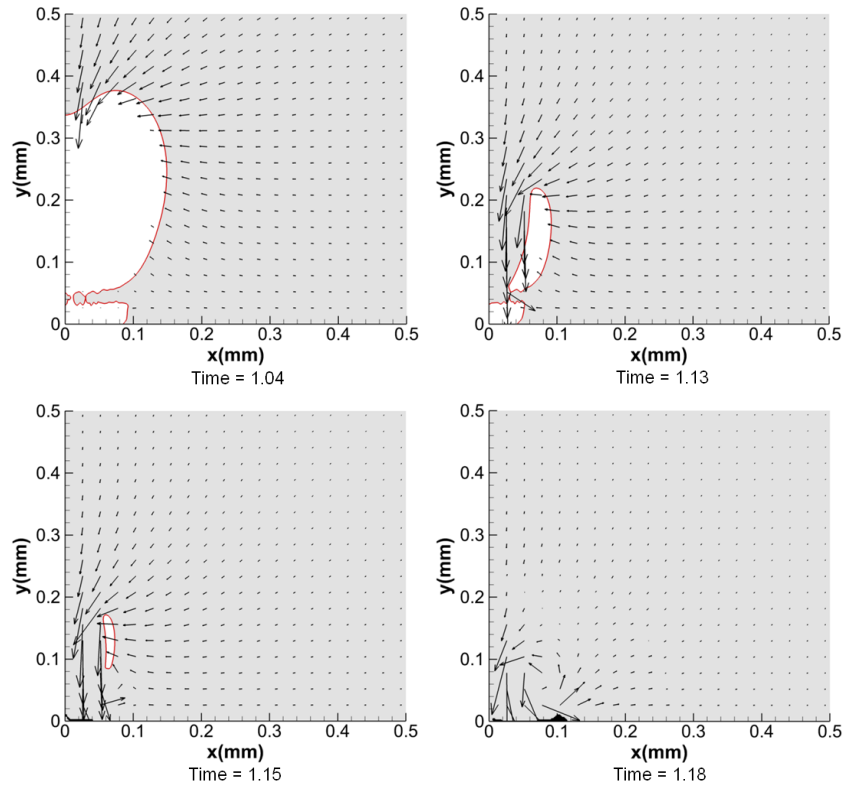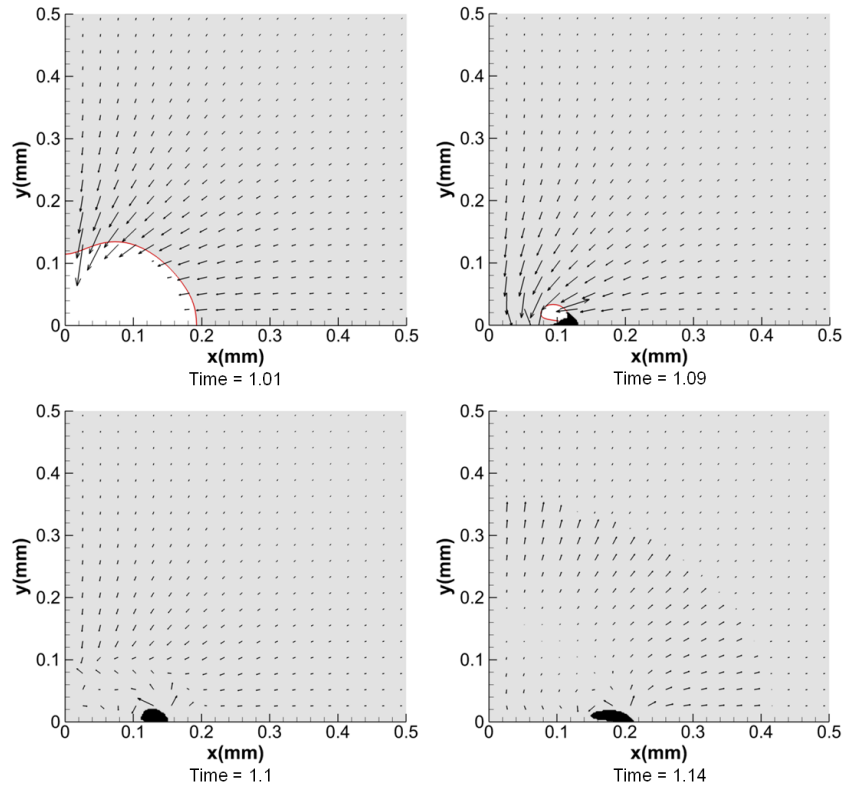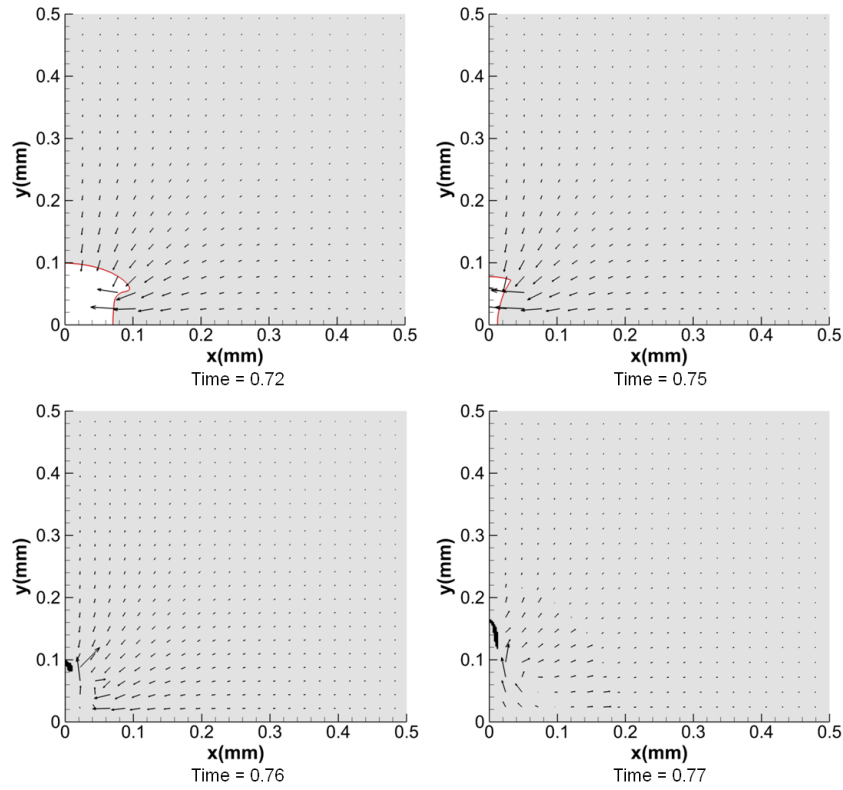**641** τ=2.88 μs.

Figure 15: Depiction of the supercritical (black), vapour (white) and liquid (grey) regions, combined with velocity vectors for d=-140 μm. Time has been non-dimensionalized with Rayleigh collapse time τ=2.88 μs.

The system-cpu time required for each thermodynamic model is compared for simulating the bubble collapse case until time 6.5 μs. The user-cpu time for the Helmholtz model is almost 3.7 times the HEM time, whereas the barotropic simulations are computationally the most efficient, as the execution time is almost 52 times smaller than the HEM time. The main reason for the increased cpu-time of the HEM model is the iterative calculation of the temperature using Newton-Raphson method, which necessitates complex expressions, especially in the mixture regime. The energy equation, which is not solved in the barotropic model, has a minor effect on the computational cost of the HEM with temperature effects.

4. Conclusions

In the present work, an explicit density-based solver with real fuel thermodynamics using the Helmholtz energy EoS has been presented. A Mach consistent numerical flux has been implemented, able to handle low as well as high Mach number flows. The numerical scheme has been validated against two benchmark test cases (Riemann problem, Rayleigh collapse); following numerical experiments for a vapour collapsing bubble near the vicinity of a wall have been performed. Since there is no analytical solution for this case or any other reference, comparison with other models has been made and areas where the fluid transitions to supercritical state have been identified. The results are satisfactory and encouraging enough in order to further expand this methodology to more realistic geometries, such as injector nozzles and expand the formulation to include non-condensable gases. The temperature variation of the fuel inside the injector can dramatically change its properties and thus affect

24

671 the flow field, which is not feasible in barotropic models, where no temperature effects exist.
672 The bilinear finite element interpolation which was chosen, is a good compromise between
673 complexity and accuracy. A posteriori error estimation was performed and error was found to
674 be less than 1% in all thermodynamic properties.
675   Although no gas phase is included in the current model and thus the heating in the inner
676 of the bubble cannot be predicted, real fluid thermodynamics are incorporated in the
677 algorithm, with the potential of predicting supercritical transitions. The barotropic model is
678 robust and can be used as a reference, but temperature effects are ignored. The HEM with
679 simplified thermodynamics, is only applicable for a small range of temperatures. On the other
680 hand, Helmholtz EoS is applicable for a wider range, as long as experimental data exist to
681 calibrate the equation. While the trend of all thermodynamic models employed is similar,
682 supercritical transitions are only possible to capture using the Helmholtz (or equivalent
683 cubic/high order EoS, such as Peng-Robinson, see (Lacaze et al., 2015)), showing the
684 importance of accurate thermodynamic modelling.

685

686 Acknowledgements

692

693 Appendix

694 Derivation of the exact Riemann Problem solution for an arbitrary equation of state of the
695 form $p=f(\rho,e)$.

697 Figure A.1. Wave structure of the Riemann problem for the Euler equations for a general equation of
698 state $p=f(\rho,e)$.

699

700   In this section, the methodology for finding the exact solution to the Riemann problem for
701 the Euler equations, for an arbitrary equation of state of the form $p=f(\rho,e)$ is derived. The
702 equation of state may be provided in closed form, where simplifications as in Toro (2009)
703 may be done, or in a general tabular form. The interested reader is also addressed to (Le
704 Métayer et al., 2005; Menikoff and Plohr, 1989; Müller et al., 2009; Müller and Voss, 2006;
705 Petitpas et al., 2009; Saurel et al., 2008; Saurel and Lemetayer, 2001). The form of the
706 Riemann problem solved is:

707

$$\begin{cases} \dfrac{\partial \mathbf{U}}{\partial t} + \dfrac{\partial \mathbf{F(U)}}{\partial x} = 0 \\ \mathbf{U}(x,0) = \begin{cases} \mathbf{U_L} & x < 0 \\ \mathbf{U_R} & x \geq 0 \end{cases} \end{cases} \tag{A.1}$$

708

709

710 where $\mathbf{U}(x,t)$ is the vector of conservative variables and $\mathbf{F(U)}$ is the flux vector, as shown
711 below:

$$U = \begin{bmatrix} \rho \\ \rho u \\ \rho E \end{bmatrix} \qquad\qquad F(U) = \begin{bmatrix} \rho u \\ \rho u^2 + p \\ u(\rho E + p) \end{bmatrix}$$

712

713 where $E = \frac{1}{2}u^2 + e$, with e the internal energy. The Jacobian matrix, $\mathbf{A(U)}$ is:

714
$$\mathbf{A(U)} = \begin{bmatrix} 0 & 1 & 0 \\ \dfrac{\partial p}{\partial \rho} + \dfrac{\dfrac{\partial p}{\partial e}\left(u^2 - 2e\right) - 2\rho u^2}{2\rho} & u\left(2 - \dfrac{\partial p}{\partial e}\right) & \dfrac{1}{\rho}\dfrac{\partial p}{\partial e} \\ -\dfrac{u\left[2p + \dfrac{\partial p}{\partial e}\left(2e - u^2\right) + \rho\left(u^2 - 2\dfrac{\partial p}{\partial \rho} + 2e\right)\right]}{2\rho} & \dfrac{\left(\rho - 2\dfrac{\partial p}{\partial e}\right)u^2 + 2p + 2e\rho}{2\rho} & \dfrac{\left(\dfrac{\partial p}{\partial e} + \rho\right)u}{\rho} \end{bmatrix}$$

715
716 and the eigenvalues $[\lambda_1, \lambda_2, \lambda_3]$ are

717
$$\lambda_1 = u - \sqrt{\dfrac{\partial p}{\partial \rho} + \dfrac{\partial p}{\partial e}\dfrac{p}{\rho^2}}$$

718
$$\lambda_2 = u$$

719
$$\lambda_3 = u + \sqrt{\dfrac{\partial p}{\partial \rho} + \dfrac{\partial p}{\partial e}\dfrac{p}{\rho^2}}$$

720   The solution of the Euler equations (A.1) is self similar, with two genuinely non-linear
721 waves, corresponding to λ_1 and λ_3 eigenvalues, that can be either shock waves or rarefaction
722 waves (Figure A.1). These waves separate the solution of the Riemann problem to the Left
723 state, the Right state and the Star state (denoted with '$*$' from now on) which is unknown; note
724 that in the star region pressure and u velocity are the same, but density and internal energy are
725 not. Density and internal energy change not only across the non-linear waves, but also along
726 the contact discontinuity (corresponding to λ_2).
727   To find the solution to the Riemann problem, one needs to solve a non-linear algebraic
728 equation for pressure:

729
$$g(p_*) = g_L(p_*) + g_R(p_*) + u_R - u_L = 0 \tag{A.2}$$

730

731   Functions g_L and g_R depend on the type of non-linear wave. For shock wave the Rankine-
732 Hugoniot conditions are employed, eventually leading to:

733
$$g_{K,shock} = \left[\dfrac{(p_* - p_K)(\rho_{*,K} - \rho_K)}{\rho_{*,K}\,\rho_K}\right]^{1/2} \tag{A.3}$$

734 for $K=L$ or R state. Apart from A.3, energy conservation applies across the shock wave, thus:

735

$$e_{*,K} = \frac{1}{2}\left(p_* + p_K\right)\left(\frac{\rho_{*,K} - \rho_K}{\rho_{*,K}\,\rho_K}\right) + e_K \tag{A.4}$$

To solve A.4 and A.3 an iterative procedure is required; initially one assumes an initial internal energy e'_{*K} (e.g. equal to e_K) which, combined with pressure p_*, corresponds to a density ρ_{*K}. This density can be used to obtain the $g_{K,shock}$ function and the internal energy from the energy balance (A.4). Since $e_{*,K}$ from (A.4) and e'_{*K} are not necessarily the same, due to the guessed value of the latter, e'_{*K} is corrected and the process is repeated till convergence.

For the rarefaction wave, the calculation is more complicated, since it involves the Riemann invariants across an isentropic path. The Riemann invariants are shown below for the left rarefaction wave:

$$du + \frac{c}{\rho}\,d\rho = 0 \;\text{ for } s=s_L \tag{A.4}$$

and for right rarefaction wave

$$du - \frac{c}{\rho}\,d\rho = 0 \;\text{ for } s=s_R \tag{A.5}$$

Integration of these relations is not convenient to be done analytically for a general equation of state, which might be expressed in tabular form. It is rather convenient to perform the integration numerically on an isentropic path across the rarefaction wave, as follows for e.g. the left rarefaction wave:

$$u_* - u_L + \int_L^* \left(\frac{c}{\rho}\right)_{s=s_L} d\rho = 0 \tag{A.6}$$

One can split the integral as follows:

$$u_* + \int_{ref}^* \left(\frac{c}{\rho}\right)_{s=s_L} d\rho = u_L + \int_{ref}^L \left(\frac{c}{\rho}\right)_{s=s_L} d\rho \tag{A.7}$$

where ref is a reference state at e.g. at the minimum allowable density of the equation of state. In a similar manner one may derive the relation for the right rarefaction wave:

$$u_* - \int_{ref}^* \left(\frac{c}{\rho}\right)_{s=s_R} d\rho = u_R - \int_{ref}^R \left(\frac{c}{\rho}\right)_{s=s_R} d\rho \tag{A.8}$$

and eventually, the function

$$g_{K,rarefaction} = \int_{ref}^* \left(\frac{c}{\rho}\right)_{s=s_K} d\rho - \int_{ref}^K \left(\frac{c}{\rho}\right)_{s=s_R} d\rho \tag{A.9}$$

Hereafter the integral $\int_{ref}^K \left(\frac{c}{\rho}\right)_{s=s_K} d\rho$ will be referred to as $I_K(p_K)$.

Calculation of the isentropic integral $I_K(p_K)$ may be done numerically. At first, one needs to calculate the states that have the same entropy, s, as the right (R) and left (L) state. Assuming that the thermodynamic properties are expressed in the form of $f(\rho,e)$, the isentropic path may be calculated as follows:

1. determine the entropy of the K state (K can be either L or R), as $s_K = s(\rho_K, e_K)$

2. starting from a low reference density, ρ_{ref}, and increasing by intervals $d\rho$, the point that corresponds to s_K is found by iteratively correcting internal energy, e, for the given path point

27

769 *i*. Internal energy correction may be done with the Newton-Raphson method, till a specified
770 tolerance is reached.

771   3. after reaching the tolerance, the rest thermodynamic properties (e.g. pressure, speed of
772 sound etc.) for (ρ_i, e_i) may be found. Speed of sound, c, is needed to evaluate the term inside
773 the integral *I*. Pressure is needed in order to express the integral as a function of pressure; this
774 is preferable, because pressure at the whole star region is the same. The integral may be
775 calculated by using the trapezoid rule, or a more accurate Simpson method. Care should be
776 taken in areas of large changes in the speed of sound, as e.g. near saturation lines.

777   4. the procedure may be done till a high pressure p_{max} which should be greater than the
778 pressure expected to appear in the rest calculations.

779   Switching between rarefaction and shock wave is done based on pressure:

$$g_K = \begin{cases} g_{K,rarefaction} & p_K < p_* \\ g_{K,shock} & p_K \geq p_* \end{cases}$$

780   (A.10)

781 The solution for the star region can be achieved with the Newton-Raphson method:

$$p_n = p_{n-1} - \frac{g(p_{n-1})}{g'(p_{n-1})} urf$$

782   (A.11)

783 where *n* is the number of the iteration, *urf* is an under-relaxation factor to enhance stability in
784 case of highly non-linear EOS and g' is the derivative of eq. A.2. Note that for such equations
785 it is preferable to resort to a numerically approximated value of the derivative, as:

$$g'(\rho) = \frac{g(\rho + \varepsilon) - g(\rho)}{\varepsilon}$$

786   (A.12)

787 where ε is a small positive number.

788   For highly non-linear EOS, it might be preferable also to bound the maximum change of
789 pressure from iteration to iteration, in order to prevent overshoots/undershoots and enhance
790 stability, i.e.:

791                          $$p_n = \max(\min(p_n, p_{max}), p_{min})$$

792 where p_{max}, p_{min} can be a percentage of density during the previous iteration, e.g. 120% and
793 80% of p_{n-1} respectively. After determining p_* within sufficient tolerance, determining
794 velocity u_* is trivial, though the following equation:

795                $$u_* = 0.5(u_L + u_R) + 0.5[g_R(p_*) - g_L(p_*)]$$ (A.13)

796   Identification of the type of waves is done depending on pressure at the star region
797 comparing to the left and right states: if $p_*>p_K$ then the wave between the star and *K* region is
798 a shock wave, else it is a rarefaction wave. The type of wave determines the wave speed and
799 the transition between the two states. For a shock wave the transition is sharp and the wave
800 speed is given by:

801   Left shock: $S_L = u_L - \dfrac{Q_L}{\rho_L}$, right shock $S_R = u_R + \dfrac{Q_R}{\rho_R}$ (A.14)

802 with

803                     $$Q_K = \left[\frac{(p_* - p_K)\rho_{*,K}\rho_*}{\rho_{*,K} - \rho_K} \right]^{1/2}$$ (A.15)

804 Rarefactions, contrary to shocks, are gradual changes in density, pressure and velocity. Thus,
805 they are associated with two speeds, one for the head of the rarefaction and one for the tail:
806

807   Left rarefaction, head: $S_{LH} = u_L - c_L$ tail: $S_{LT} = u_* - c_{*,L}$ (A.16)

808   Right rarefaction, head: $S_{RH} = u_R + c_R$ tail: $S_{RT} = u_* + c_{*,R}$ (A.17)

809 In order to find the conditions inside the rarefaction wave, the Riemann invariants shall be
810 used. For a left rarefaction, one has to solve the following equation for the point i inside the
811 rarefaction:

812
$$\frac{x_i}{t} + c(p_i) + I_L(p_i) = u_L + I_L(p_L) \qquad \text{(A.18)}$$

813 Similarly, for the right rarefaction

814
$$\frac{x_i}{t} - c(p_i) - I_R(p_i) = u_R - I_R(p_R) \qquad \text{(A.19)}$$

815 Solution of eq. A.18 and A.19 can be done numerically, solving for density, using
816 Newton-Raphson method, applying under-relaxation and taking care during the updating of
817 the density values. Experience has shown that it is better to apply a low under-relaxation
818 factor of even 0.02.

819 Assuming the dodecane Helmholtz EOS and assuming an initial discontinuity of the form
820 ρ_L=752.5kg/m^3 and temperature T_L=289K for x<0, ρ_R=717.5kg/m^3 and T_R=350K for x≥0
821 (which corresponds to p_L~44330Pa and p_R~109bar), one obtains that the solution of the
822 Riemann problem at the star region is:

823 $$p_* = 6017572\text{Pa}, \ u_* = \text{-}5.94\text{m/s}$$
824 $$\rho_{*,L} = 755.86\text{kg/m}^3, \ \rho_{*,R} = 713.48\text{kg/m}^3$$
825 $$T_{*,L} = 290.02\text{K}, \ T_{*,R} = 349.47\text{K}$$

826 With rarefaction wave to the right S_{TR}=1125.13m/s, S_{HR}=1162.62m/s and shock wave to left
827 S_L=-1336.49m/s.

828

829 **References**

830 Adams, N.A., Schmidt, S.J., 2013. Shocks in Cavitating Flows, in: Delale, F.C. (Ed.), Bubble
831   Dynamics and Shock Waves. Springer Berlin Heidelberg, Berlin, Heidelberg, pp. 235-256.
832 Brennen, C.E., 1995. Cavitation and Bubble Dynamics.
833 Chahine, G., 2014. Modeling of Cavitation Dynamics and Interaction with Material. Springer
834   Netherlands, pp. 123-161.
835 Decaix, J., Goncalvès, E., 2013. Compressible effects modeling in turbulent cavitating flows.
836   European Journal of Mechanics - B/Fluids 39, 11-31.
837 Dular, M., Coutier-Delgosha, O., 2009. Numerical modelling of cavitation erosion. Int. J.
838   Numer. Meth. Fluids 61, 1388-1410.
839 Dumbser, M., Iben, U., Munz, C.-D., 2013. Efficient implementation of high order
840   unstructured WENO schemes for cavitating flows. Computers & Fluids 86, 141-168.
841 Egerer, C.P., Hickel, S., Schmidt, S.J., Adams, N.A., 2014. Large-eddy simulation of turbulent
842   cavitating flow in a micro channel. Physics of Fluids 26, 085102.
843 Franc, J.P., Michel, J.M., 2005. Fundamentals of Cavitation. Kluwer Academic Publishers.
844 Glimm, J., Klingenberg, C., McBryan, O., Plohr, B., Sharp, D., Yaniv, S., 1985. Front tracking
845   and two-dimensional Riemann problems. Advances in Applied Mathematics 6, 259–290.
846   doi:10.1016/0196-8858(85)90014-4
847 Guillard, H., Viozat, C., 1999. On the behaviour of upwind schemes in the low Mach number
848   limit. Computers & Fluids 28, 63-86.
849 Hawker, N.A., Ventikos, Y., 2009. Shock/Gas bubble interactions in infinite and finite
850   volumes of liquid, 2nd Micro and Nano Flows Conference, West London, UK.
851 Hawker, N.A., Ventikos, Y., 2012. Interaction of a strong shockwave with a gas bubble in a
852   liquid medium: a numerical study. Journal of Fluid Mechanics 701, 59-97.
853 Hu, X.Y., Khoo, B.C., Adams, N.A., Huang, F.L., 2006. A conservative interface method for
854   compressible flows. Journal of Computational Physics 219, 553-578.

855   Koop, A.H., 2008. Numerical Simulation of Unsteady Three-Dimensional Sheet Cavitation.
856   University of Twente.

857   Koukouvinis, P., Gavaises, M., 2015. Simulation of throttle flow with two phase and single
858   phase homogenous equilibrium model. Journal of Physics: Conference Series 656,
859   012086.

860   Koukouvinis, P., Gavaises, M., Georgoulas, A., Marengo, M., 2016a. Compressible
861   simulations of bubble dynamics with central-upwind schemes. International Journal of
862   Computational Fluid Dynamics, 1-12.

863   Koukouvinis, P., Gavaises, M., Supponen, O., Farhat, M., 2016b. Numerical simulation of a
864   collapsing bubble subject to gravity. Physics of Fluids 28, 032110.

865   Koukouvinis, P., Gavaises, M., Supponen, O., Farhat, M., 2016c. Simulation of bubble
866   expansion and collapse in the vicinity of a free surface. Physics of Fluids 28, 052103.

867   Lacaze, G., Misdariis, A., Ruiz, A., Oefelein, J.C., 2015. Analysis of high-pressure Diesel fuel
868   injection processes using LES with real-fluid thermodynamics and transport. Proceedings
869   of the Combustion Institute 35, 1603-1611.

870   Lauer, E., Hu, X.Y., Hickel, S., Adams, N.A., 2012. Numerical modelling and investigation of
871   symmetric and asymmetric cavitation bubble dynamics. Computers & Fluids 69, 1-19.

872   Lemmon, E.W., Huber, M.L., 2004. Thermodynamic Properties of n-Dodecane. Energy &
873   Fuels 18, 960-967.

874   Le Métayer, O., Massoni, J., Saurel, R., 2005. Modelling evaporation fronts with reactive
875   Riemann solvers. Journal of Computational Physics 205, 567–610. doi:10.1016/j.jcp.2004.
876   11.021

877   Li, B.B., Jia, W., Zhang, H.C., Lu, J., 2014. Investigation on the collapse behavior of a
878   cavitation bubble near a conical rigid boundary. Shock Waves 24, 317-324.

879   Meister, A., 1999. Asymptotic Single and Multiple Scale Expansions in the Low Mach Number
880   Limit. SIAM Journal on Applied Mathematics 60, 256-271.

881   Meng-Sing, L., 2006. A sequel to AUSM, Part II: AUSM$^+$-up for all speeds. Journal of
882   Computational Physics 214, 137-170.

883   Menikoff, R., Plohr, B., 1989. The Riemann problem for fluid flow of real materials.
884   Rev.Mod.Phys. 61, 75–130.

885   Müller, S., Bachmann, M., Kröninger, D., Kurz, T., Helluy, P., 2009. Comparison and validation
886   of compressible flow simulations of laser-induced cavitation bubbles. Computers & Fluids
887   38, 1850–1862. doi:10.1016/j.compfluid.2009.04.004

888   Müller, S., Voss, A., 2006. The Riemann Problem for the Euler Equations with Nonconvex and
889   Nonsmooth Equation of State: Construction of Wave Curves. SIAM J. Sci. Comput. 28, 651-
890   681. doi:10.1137/040619909

891   Munz, C.D., Roller, S., Klein, R., Geratz, K.J., 2003. The extension of incompressible flow
892   solvers to the weakly compressible regime. Computers & Fluids 32, 173-196.

893   Obreschkow, D., Kobel, P., Dorsaz, N., de Bosset, A., Nicollier, C., Farhat, M., 2006. Cavitation
894   Bubble Dynamics inside Liquid Drops in Microgravity. Physical Review Letters 97, 094502.

895   Obreschkow, D., Tinguely, M., Dorsaz, N., Kobel, P., de Bosset, A., Farhat, M., 2013. The
896   quest for the most spherical bubble: experimental setup and data overview. Experiments
897   in Fluids 54, 1-18.

898   Petitpas, F., Massoni, J., Saurel, R., Lapebie, E., Munier, L., 2009. Diffuse interface model for
899   high speed cavitating underwater systems. International Journal of Multiphase Flow 35,
900   747–759. doi:10.1016/j.ijmultiphaseflow.2009.03.011

901   Plesset, M.S., Chapman, R.B., 1971. Collapse of an initially spherical vapour cavity in the
902   neighbourhood of a solid boundary. Journal of Fluid Mechanics 47, 283-290.

903   Popinet, S.T., Eacute, Phane, Zaleski, S.T., Eacute, Phane, 2002. Bubble collapse near a solid
904   boundary: a numerical study of the influence of viscosity. Journal of Fluid Mechanics 464,
905   137-163.

906 Pozrikidis, C., 2009. Fluid Dynamics: Theory, Computation, and Numerical Simulation:
907   Accompanied by the Software Library FDLIB. Springer Science & Business Media.
908 Saurel, R., Lemetayer, O., 2001. A multiphase model for compressible flows with interfaces,
909   shocks, detonation waves and cavitation. Journal of Fluid Mechanics 431, 239–271.
910   doi:10.1017/S0022112000003098
911 Saurel, R., Petitpas, F., Abgrall, R., 2008. Modelling phase transition in metastable liquids:
912   application to cavitating and flashing flows. Journal of Fluid Mechanics 607, 313–350.
913   doi:10.1017/S0022112008002061
914 Schmidt, S., Sezal, I., Schnerr, G., Talhamer, M., 2008. Riemann Techniques for the
915   Simulation of Compressible Liquid Flows with Phase-transition at all Mach numbers-Shock
916   and Wave Dynamics in Cavitating 3-D Micro and Macro Systems, AIAA Aerospace Sciences
917   Meeting and Exhibit.
918 Schmidt, S.J., 2005. Ein Verfahren zur präzisen Berechnung dreidimensionaler, reibungsfreier
919   Idealgasströmungen über dem gesamten Kompressibilitätsbreich. Technische Universität
920   München, Munich.
921 Schmidt, S.J., Sezal, I.H., Schnerr, G.H., 2006. Compressible simulation of high-speed
922   hydrodynamics with phase change, in: P. Wesseling, E.O.a.J.P. (Ed.), European Conference
923   on Computational Fluid Dynamics, TU Delft.
924 Toro, E., 2009. Riemann Solvers and Numerical Methods for Fluid Dynamics: A Practical
925   Introduction. Springer Berlin Heidelberg, Berlin, Heidelberg.
926 Unverdi, S.O., Tryggvason, G., 1992. A front-tracking method for viscous, incompressible,
927   multi-fluid flows. Journal of Computational Physics 100, 25-37.
928 Van der Heul, D.R., Vuik, C., Wesseling, P., 2000. Efficient computation of flow with
929   cavitation by compressible Pressure Correction, European Conference on Computational
930   Fluid Dynamics, Barcelona.
931 Wang, Q., 2014. Multi-oscillations of a bubble in a compressible liquid near a rigid boundary.
932   Journal of Fluid Mechanics 745, 509-536.
933 Zhang, S., Duncan, J.H., Chahine, G.L., 1993. The final stage of the collapse of a cavitation
934   bubble near a rigid wall. Journal of Fluid Mechanics 257, 147-181.
935 Zhang, S., Duncan, J.H., Chahine, G.L., 1994. The behavior of a cavitation bubble near a rigid
936   wall, in: Blake, J.R., Boulton-Stone, J.M., Thomas, N.H. (Eds.), Bubble Dynamics and
937   Interface Phenomena: Proceedings of an IUTAM Symposium held in Birmingham, U.K., 6–9
938   September 1993. Springer Netherlands, Dordrecht, pp. 429-436.

939